KeAi

ISSN 2452-199X (Online)
ISSN 2097-1192 (Print)
CN 10-1775/Q
生物活性材料（英文）

BIOACTIVE MATERIALS

Volume 31 • January 2024

Rapid and effective treatment of chronic osteomyelitis by conductive network-like MoS2/CNTs through multiple reflection and scattering enhanced synergistic therapy
pp. 284-297

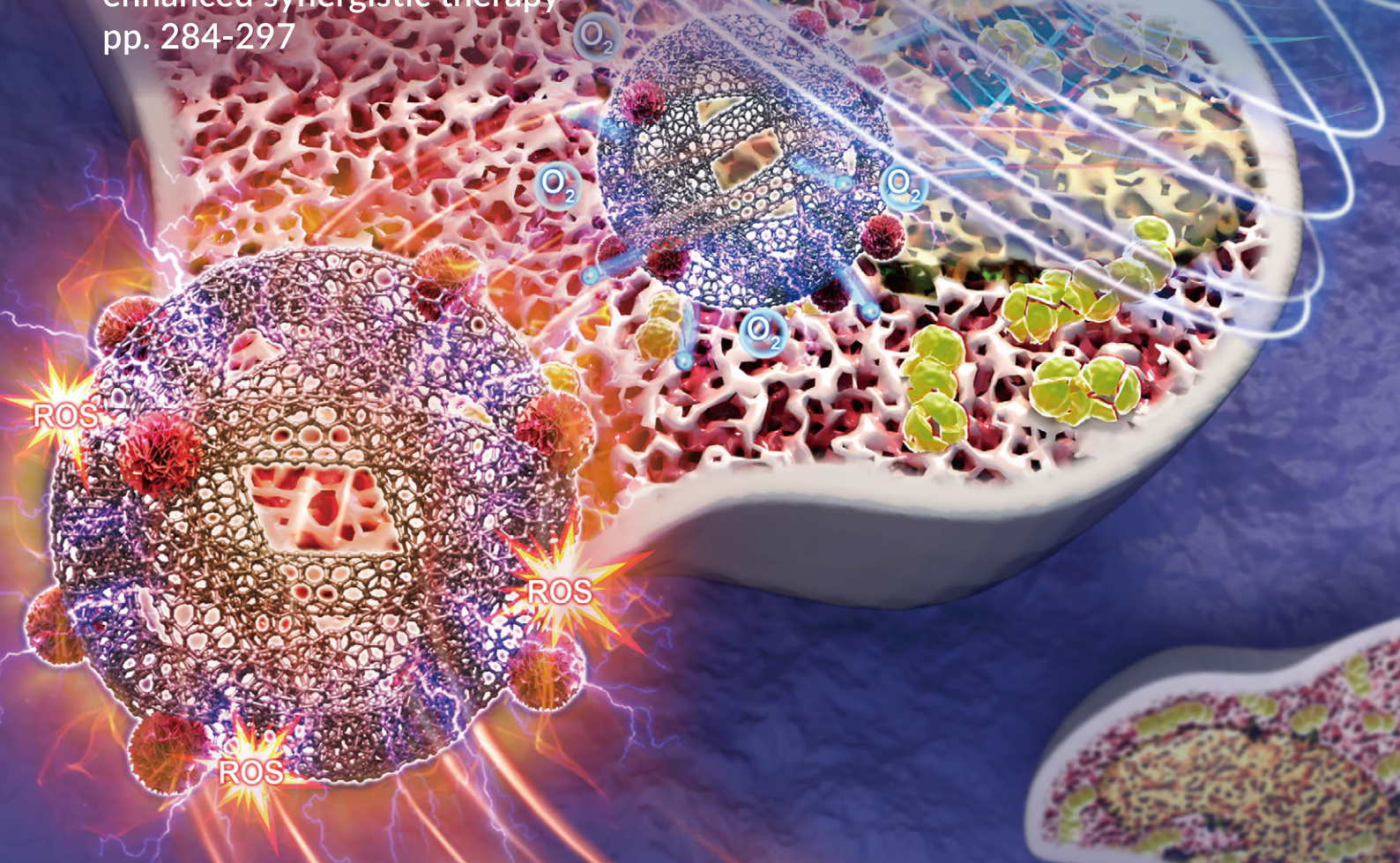

IMPACT FACTOR 2022: 18.9

CiteScore 2022: 19.7

ScienceDirect
Available online at www.sciencedirect.com

Actions for selected articles

Select all / Deselect all

Download PDFs

Export citations

Show all article previews

Research article • *Open access*

3D-printed tri-element-doped hydroxyapatite/ polycaprolactone composite scaffolds with antibacterial potential for osteosarcoma therapy and bone regeneration

Hao Huang, Lei Qiang, Minjie Fan, Yihao Liu, ... Jie Weng

Pages 18-37

View PDF Article preview

Research article • *Open access*

Bilayer vascular grafts with on-demand NO and H_2S release capabilities

Pengfei Li, Fubang Liang, Lijuan Wang, Dawei Jin, ... Meng Yin

Pages 38-52

View PDF Article preview

Review article • *Open access*

Manganese molybdate nanodots with dual amplification of STING activation for “cycle” treatment of metalloimmunotherapy

Huali Lei, Quguang Li, Guangqiang Li, Tianyi Wang, ... Liang Cheng

Bioactive Materials 31 (2024) 18–37

Contents lists available at ScienceDirect

Bioactive Materials

journal homepage: www.keaipublishing.com/en/journals/bioactive-materials

3D-printed tri-element-doped hydroxyapatite/ polycaprolactone composite scaffolds with antibacterial potential for osteosarcoma therapy and bone regeneration

Hao Huang [a,1], Lei Qiang [a,b,c,1], Minjie Fan [b,1], Yihao Liu [b,c], Anchun Yang [a], Dongbiao Chang [a], Jinsheng Li [a], Tong Sun [a], Yiwei Wang [b], Ruoyi Guo [b], Hanjie Zhuang [b], Xiangyu Li [c,d], Tailin Guo [a], Jinwu Wang [c], Huan Tan [a,***], Pengfei Zheng [b,**], Jie Weng [a,*]

[a] Key Laboratory of Advanced Technologies of Materials (MOE), School of Materials Science and Engineering, College of Medicine, Southwest Jiaotong University, Chengdu, 610031, PR China
[b] Department of Orthopaedic Surgery, Children's Hospital of Nanjing Medical University, Nanjing 210008, PR China
[c] Shanghai Key Laboratory of Orthopedic Implant, Department of Orthopedic Surgery Shanghai Ninth People's Hospital, Shanghai Jiao Tong University School of Medicine Shanghai 200011, PR China
[d] School of Mechanical and Electrical Engineering, Henan University of Technology, Zhengzhou 450001, PR China

ARTICLE INFO

Keywords:
Element-doped HA-PCL scaffolds
3D printing
Osteogenic
Osteosarcoma
Antibacterial

ABSTRACT

The resection of malignant osteosarcoma often results in large segmental bone defects, and the residual cells can facilitate recurrence. Consequently, the treatment of osteosarcoma is a major challenge in clinical practice. The ideal goal of treatment for osteosarcoma is to eliminate it thoroughly, and repair the resultant bone defects as well as avoid bacterial infections. Herein, we fabricated a selenium/strontium/zinc-doped hydroxyapatite (Se/Sr/Zn-HA) powder by hydrothermal method, and then employed it with polycaprolactone (PCL) as ink to construct composite scaffolds through 3D printing, and finally introduced them in bone defect repair induced by malignant osteosarcoma. The resultant composite scaffolds integrated multiple functions involving anti-tumor, osteogenic, and antibacterial potentials, mainly attributed to the anti-tumor effects of SeO_3^{2-}, osteogenic effects of Sr^{2+} and Zn^{2+}, and antibacterial effects of SeO_3^{2-} and Zn^{2+}. *In vitro* studies confirmed that Se/Sr/Zn-HA leaching solution could induce apoptosis of osteosarcoma cells, differentiation of MSCs, and proliferation of MC3T3-E1 while showing excellent antibacterial properties. *In vivo* tests demonstrated that Se/Sr/Zn-HA could significantly suppress tumors after 8 days of injection, and the Se/Sr/Zn-HA-PCLs scaffold repaired femoral defects effectively after 3 months of implantation. Summarily, the Se/Sr/Zn-HA-PCLs composite scaffolds developed in this study were effective for tumor treatment, bone defect repair, and post-operative anti-infection, which provided a great potential to be a facile therapeutic material for osteosarcoma resection.

1. Introduction

Osteosarcoma is derived from primitive mesenchymal cells in the bone accompanying with characterization of easy metastasis, local pain, high recurrence, and drug resistance [1,2]. Osteosarcoma is a common malignant bone tumor that mainly occurs in children and adolescents and has become the second leading cause of cancer-related death in adolescents [3,4]. The main treatment methods for osteosarcoma include surgical resection, chemotherapy, and radiotherapy, while bone defects caused by osteosarcoma are often repaired by autologous bone transplantation [5–7]. However, surgical resection can not completely eliminate residual bone tumor cells at the lesion site, which can reproliferate and metastasize, increasing the risk of tumor recurrence. In addition, osteosarcoma is not responsive to radiotherapy and has a high

Peer review under responsibility of KeAi Communications Co., Ltd.
* Corresponding author.
** Corresponding author.
*** Corresponding author.
E-mail addresses: tanhuan@swjtu.edu.cn (H. Tan), zhengpengfei@njmu.edu.cn (P. Zheng), jweng@swjtu.edu.cn (J. Weng).
[1] The authors wish it to be known that, in their opinion, the first three authors should be regarded as joint First Authors.

https://doi.org/10.1016/j.bioactmat.2023.07.004
Received 9 March 2023; Received in revised form 3 July 2023; Accepted 5 July 2023
Available online 4 August 2023

tendency to develop chemotherapy resistance [3,8]. Autologous bone transplantation for the treatment of bone defects caused by osteosarcoma resection is an alternative but it has several issues, such as donor site complications, immune rejection, and limited supply, thus limiting its clinical application [2,9,10]. Therefore, there is an urgent demand for a multifunctional artificial bone substitute that can repair the bone defects caused by osteosarcoma while eliminating cancer cell and inhibiting bacterial infections [11].

Hydroxyapatite (HA) is the main inorganic component of hard human tissues and is widely used in bone tissue engineering due to its excellent biocompatibility, osteoconductivity, and biological activity [12–14]. In addition, HA can be adopted as a gene and small molecule drug carrier to induce the osteogenic differentiation of stem cells and bone defect repair [15,16]. Recent studies have found that nano-HA can induce apoptosis of various cancer cells, which shows an excellent anticancer effect without affecting normal cells [17]. However, the implanted materials toward repairing bone defects in load-bearing parts are required with good osteogenic capacity and mechanical properties. Related studies have shown that HA of whisker-like and microspheres can transmit and withstand larger loads than most nanoparticles [18]. Zhang et al. confirmed that micro-HA displayed better dispersibility in composites and better ability to enhance the strength and toughness of composites than that of nano-HA particles [19]. Meanwhile, trace elements play an important role in the growth and development of human bone tissue and are integral to the daily activities of the body [20,21]. Different trace elements play different roles in the growth and development of bone tissue. For example, zinc (Zn), manganese (Mn), and strontium (Sr) have good osteogenic effects; magnesium (Mg), copper (Cu) as well as cobalt (Co) contain excellent angiogenic effects; silicon (Si) and boron (B) possess osteogenic and angiogenic effects; selenium (Se) can promote bone tissue development and anti-aging [22–24]. Several studies have confirmed that trace elements can control the degradation of calcium phosphate materials and improve their biological functions [22]. Zn-doped HA (Zn-HA) had better osteogenic properties and antibacterial effects than pure HA [25,26]. Sr-doped HA (Sr-HA) demonstrated excellent therapeutic effects on osteoporosis and showed the potential for antibacterial activity during bone repair [27,28]. Zhang et al. confirmed that oral strontium ranelate combined with HA porous scaffold implantation provided better osteoporosis treatment effects than Sr-HA porous scaffold implantation [29]. Se helps reduce reactive oxygen species-mediated inflammation, reduces DNA damage, and increases telomere length, which plays crucial roles in anti-aging and preventing aging-related diseases [30]. Furthermore, Se-doped HA (Se-HA) has better anti-tumor and osteogenic effects compared with HA [31–33]. However, it is difficult to repair bone defects caused by osteosarcoma while treating osteosarcoma using single-element doped HA. Instead, multi-element synergistic doping of HA is effective alternative for the repair of bone defects because of its multifunctional nature. To the best of our knowledge, there are limited studies on the three-element doping HA for treatment of osteosarcoma, bone defect repair, and postoperative anti-infection in an integrated material. Therefore, this study aimed to design and fabricate a multifunctional scaffold to eliminate tumors, repair bone defects, and antagonize bacterial infections after osteosarcoma resection.

As shown in Fig. 1, the Se/Sr/Zn-doped HA (Se/Sr/Zn-HA) was synthesized using the hydrothermal method. Subsequently, the Se/Sr/Zn-HA and polycaprolactone (PCL) composite scaffolds (Se/Sr/Zn-HA-PCLs) were fabricated by 3D printing technology. The *in vitro* and *in vivo* anti-tumor properties of Se/Sr/Zn-HA were determined by assessing the activities of tumor cells and the subcutaneous tumor model of nude mice. The activities and osteogenic differentiation potential of stem cells *in vitro* confirmed the osteogenic differentiation potential of Se/Sr/Zn-HA, and the rat femoral defect model was used to verify the osteogenic effects of Se/Sr/Zn-HA-PCLs. Furthermore, the antibacterial properties of Se/Sr/Zn-HA were studied and compared with the single element doped HA.

2. Materials and methods

2.1. Materials

Calcium nitrate tetrahydrate [$Ca(NO_3)_2{\cdot}4H_2O$, AR], zinc nitrate hexahydrate [$Zn(NO_3)_2{\cdot}6H_2O$, AR], strontium nitrate [$Sr(NO_3)_2$], sodium selenite (Na_2SeO_3, AR), phosphoric acid dodecahydrate disodium hydrogen ($Na_2HPO_4{\cdot}12H_2O$, AR), nitric acid (HNO_3, AR), glutaraldehyde ($C_5H_8O_2$, AR), urea (CH_4N_2O, AR) and absolute ethanol (AR) were purchased from Chengdu Kelong Chemical Reagent Factory. Phosphate buffered saline (PBS) and bovine serum albumin (BSA) were purchased from Amreco (USA), BCA kit, Western and IP cell lysate, alkaline phosphatase assay kit (*ALP*), and CCK-8 cell proliferation and toxicity The detection kit (CCK-8) was provided by Biyuntian Biotechnology Co., Ltd. (Shanghai, China). Rhodamine-labeled phalloidin (TRITC Phalloidin) and DAPI staining solution ($C_{16}H_{17}C_{12}N_5{\cdot}2HCL$) were purchased from Yisheng Biotechnology Co., Ltd. (Shanghai, China). α-MEM medium (α-MEM), DMEM medium (DMEM), trypsin (Try), fetal bovine serum (FBS), and penicillin-streptomycin solution were purchased from

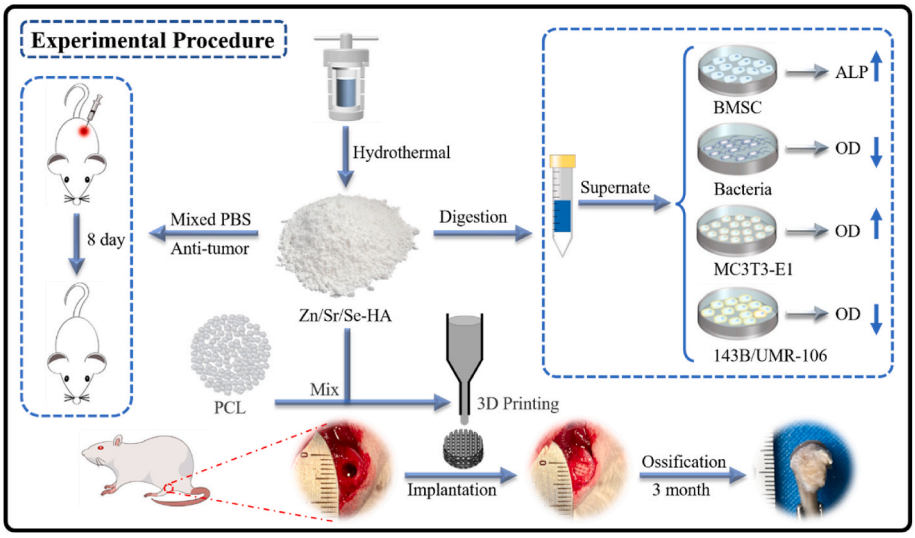

Fig. 1. Schematic diagram of the preparation and function of Se/Sr/Zn-HA and Se/Sr/Zn-HA-PCLs for tumor treatment, bone defect repair, and antibacterial.

Hyclone (USA), dimethyl sulfoxide (DMSO)), β-glycerophosphate (β-GP), dexamethasone (Dex) and vitamin C were purchased from Sigma (USA), Rhodamine B was purchased from Kasei Industry Co., Ltd. (Tokyo, Japan), polyethylene Diol octyl phenyl ether (Triton X-100) was purchased from Aladdin (USA), and Alamar Blue Cell Viability Assay Kit (AB) was purchased from Thermo (USA). Annexin V apoptosis detection kits were purchased from Becton, Dickinson, and Company (USA), beef extract powder was purchased from BioFROXX (Germany), live and dead cell viability/toxicity detection kits were purchased from KGI Biotechnology Co., Ltd. (Jiangsu, China), agar [$(C_{12}H_{18}O_9)_n$], sodium chloride (NaCl) and peptone were purchased from Jinshan Chemical Reagent Co., Ltd. (Chengdu, China). Deionized water was provided by the Key Laboratory of Materials, Southwest Jiaotong University. Dichloromethane was provided by Zhiyuan Chemical Reagent Co. LTD (MW = 84.93, Tianjin, China). PCL was purchased from Macklin Biochemical Technology Co., Ltd. (MW = 45,000, Shanghai, China). All reagents were used without further purification unless mentioned especially.

2.2. Synthesis of HA and element-doped HA

Several HA powders mentioned in this research were prepared by a hydrothermal method as reported previously [34]. In brief, to prepare Se-doped HA with designed [Se/(Se + P)] molar ratios of 5%, [denoted as Se-HA], $Ca(NO_3)_2$, Na_2SeO_3, and Na_2HPO_4 were sequentially added into 300 mL of deionized water, while the molar ratio of Ca/(Se + P) in above solution was 1.67. To prepare Sr-doped, Zn-doped HA power with designed [X/(X + Ca)] molar ratios of 10%, and 15% (X was Sr or Zn, respectively, denoted as Sr-HA and Zn-HA), $Ca(NO_3)_2$, $Sr(NO_3)_2$, and Na_2HPO_4 were sequentially added into 300 mL of deionized water, while the molar ratio of (Ca + Sr)/P in above solution was 1.67, and the fabrication of Zn-doped HA was similar to that of Sr-doped HA. To prepare Se/Sr/Zn-doped HA designed to a molar ratio with [Se/(Se + P) = 5%, Sr/(Sr + Zn + Ca) = 10%, Zn/(Sr + Zn + Ca) = 15%, denoted as Se/Sr/Zn-HA], $Ca(NO_3)_2$, $Sr(NO_3)_2$, $Zn(NO_3)_2$, Na_2SeO_3, and Na_2HPO_4 were sequentially added into 300 mL of deionized water, while the molar ratio of (Ca + Sr + Zn)/(Se + P) in above solution was 1.67. The two-element doping ratio of Se/Sr-HA, Se/Zn-HA, and Sr/Zn-HA were the same as that of single-element doping HA, which was a pairwise combination of one-element doping. The above-prepared solutions were all magnetically stirred, and the Ca^{2+} was 0.1 M. Then, the pH of the mixture was adjusted to 2.3 with HNO_3 (10.83 M), followed by addition of urea (0.56 M). After the urea was dissolved completely, the above-prepared solutions were transferred to six-station Teflon autoclaves (Xataikang, Xi'an, China) for reaction (150 °C, 3 h), and collected the precipitates when the reactions terminated. The obtained precipitates were rinsed by centrifuging (4000 rpm, 2 min) with deionized water until the pH value reached neutral, and finally rinsed with absolute ethanol for dehydration, and put into an oven (70 °C, 48 h) for drying. The un-doped HA was fabricated in the same method.

2.3. 3D printing of HA-PCLs, Se-HA-PCLs, Sr-HA-PCLs, Zn-HA-PCLs, and Se/Sr/Zn-HA-PCLs

A 3D porous composite scaffold was fabricated using a 3D biological printer (Bio-Architect® WS, REGENOVO) under the guidance of an auxiliary computer workstation. Before printing, 0.5 mg of HA, Se-HA, Sr-HA, Zn-HA, and Se/Sr/Zn-HA were dispersed in 40 mL of dichloromethane and stirred to form uniform dispersion, respectively. Then, the dispersion was added into a PCL solution (4.5 g of PCL in certain amount of dichloromethane) and fully stirred for 3 h to form a uniform ink. Afterwards, the prepared ink was extruded through a conical plastic nozzle (G27, 0.2 mm) at a speed of 5 mm/s at a pressure of 0.2 MPa to obtain a porous 3D scaffold. Finally, the 3D-printed HA-PCLs, Se-HA-PCLs, Sr-HA-PCLs, Zn-HA-PCLs, and Se/Sr/Zn-HA-PCLs were freeze-dried for 24 h to remove the organic solvent. The fidelity of HA-PCLs, Se-HA-PCLs, Sr-HA-PCLs, Zn-HA-PCLs, and Se/Sr/Zn-HA-PCLs was calculated according to the following formula (1):

$$\text{Fidelity}\ (\%) = \left[1 - \left|\frac{L_1 - L_2}{L_2}\right|\right] \times 100\% \quad (1)$$

where L_1 represented the actual side length of the pore, and L_2 represented the theoretical side length (350 μm) of the pore.

2.4. Sample characterization

The morphology, elements, and phase compositions of the samples were examined by scanning electron microscopy (SEM, JSM7800F) equipped with Energy Dispersive X-Ray Spectroscopy (EDS) and X-ray diffraction (XRD, Philips PW 3040/60, Cu-Kα, 35 mA, 45 kV), respectively. The chemical structure and Zeta potential were examined by Fourier transform infrared spectroscopy (FTIR, 500-3500 cm^{-1}, Thermo Nicolet 5700) and Laser particle size analyzer (PSA 1190, Austria), respectively. A microcomputer controlled electronic universal testing machine (WDW-5, Bairoe, China) was used for compression testing, and the stress and strain curves were monitored to calculate the compression modulus. A scaffold with a size of H 5 mm × Φ 6 mm (H × Φ) was compressed to 60% strain at a speed of 60 mm/min. The compression modulus was determined by drawing a compressive stress-strain curve for each scaffold (n = 4). Doping quantity, presence, and valence states were tested by an X-ray fluorescence spectrometer (XRF, PANalytical Axios FAST, Panaco Netherlands) and X-ray photoelectron spectroscopy (XPS, AXIS Ultra DLD, Kratos England), respectively. The release quantity of doping element in the extracts of samples was determined by inductively coupled plasma atomic emission spectra (ICP-AES, Spectro Arcos, Speicher Germany). Crystal crystallinity, cell volume, grain size, and the calcium-phosphorus ratio of samples were calculated and analyzed by Jade 6 (Materials Data, America). The actual doping efficiency and theoretical doping efficiency of the element were calculated according to the following formulas (2)-(7):

$$\text{Actual doping of Se}(\chi_{\alpha-Se}) = \frac{n(Se)_{actual}}{n(P)_{actual} + n(Se)_{actual}} \times 100\% \quad (2)$$

$$\text{Actual doping of Sr}(\chi_{\alpha-Sr}) = \frac{n(Sr)_{actual}}{n(Ca)_{actual} + n(Zn)_{actual} + n(Sr)_{actual}} \times 100\% \quad (3)$$

$$\text{Actual doping of Zn}(\chi_{\alpha-Zn}) = \frac{n(Zn)_{actual}}{n(Ca)_{actual} + n(Zn)_{actual} + n(Sr)_{actual}} \times 100\% \quad (4)$$

$$\text{Theoretical doping of Se}(\chi_{t-Se}) = \frac{n(Se)_{theoretical}}{n(P)_{theoretical} + n(Se)_{theoretical}} \times 100\% \quad (5)$$

$$\text{Theoretical doping of Sr}(\chi_{t-Sr}) = \frac{n(Sr)_{theoretical}}{n(Ca)_{theoretical} + n(Zn)_{theoretical} + n(Sr)_{theoretical}} \times 100\% \quad (6)$$

$$\text{Theoretical doping of Zn}(\chi_{t-Zn}) = \frac{n(Zn)_{theoretical}}{n(Ca)_{theoretical} + n(Zn)_{theoretical} + n(Sr)_{theoretical}} \times 100\% \quad (7)$$

Where n $(Ca)_{actual}$, n $(Se)_{actual}$, n $(Sr)_{actual}$, and n $(Zn)_{actual}$ represented the actual contents of Ca, Se, Sr, and Zn in the sample respectively, n $(Ca)_{theoretical}$, n $(Se)_{theoretical}$, n $(Sr)_{theoretical}$, and n $(Zn)_{theoretical}$ represented the theoretical contents of Ca, Se, Sr, and Zn in the sample, respectively.

2.5. In vitro ion release of element-doped HA, Se-HA-PCLs, Sr-HA-PCLs, Zn-HA-PCLs, and Se/Sr/Zn-HA-PCLs

300 mg of the corresponding HA powders were dispersed into 60 mL of phosphate buffered saline (PBS) followed by ultrasound for 20 min. Then, the solutions were kept in a thermostatic oscillator (SHZ-82A, Aohua Instrument, Changzhou) and were centrifuged at specific time intervals of 12 h, 24 h, 48 h, 96 h, and 168 h. After centrifugation, 10 mL of supernatant was harvested, and 10 mL of fresh PBS was added to the centrifuge tube and continued shaking until the release process was finished.

To simulate the degradation of composite scaffolds in a tumor environment and verify the anti-tumor potential of composite scaffolds, 0.04 g of the related samples of Se-HA-PCLs, Sr-HA-PCLs, Zn-HA-PCLs, and Se/Sr/Zn-HA-PCLs were put into 40 mL of acidic PBS (pH = 5.5), and were shaken in a shaker (100 rpm, 37 °C) for 7 days, respectively. The supernatant of acidic PBS was collected at specific time intervals and tested by Inductively Coupled Plasma Atomic Emission Spectroscopy (ICP-AES, Spectro Arcos, Speicher, Germany).

2.6. Protein adsorption assay

10 mg of samples were added to a centrifuge tube containing 1 mL of PBS solution and were dispersed uniformly by ultrasound (20 min). Subsequently, 1 mg of bovine serum albumin (BSA) adsorption solution was added and stirred evenly, and was centrifuged (10,000 rpm, 10 min) after shaking in a thermostatic oscillator (37 °C, 24 h). The BCA kit was employed to determine the concentration of BSA protein in the supernatant and calculated the amount of BSA protein adsorbed by the samples according to formula (8). A microplate reader (wavelength = 562 nm) was used to detect the optical density (OD) of each group and calculated the BSA protein concentration in the supernatant according to formula (9).

$$\text{Absorbed protein amount (AP)} = \text{Total protein} - \text{Supernatant protein amount} \tag{8}$$

Total protein was the amount of BSA protein in the centrifuge tube before conducting the protein adsorption assay, supernatant protein amount was the amount of BSA protein that was not adsorbed after the experiment.

$$\text{Protein concentration } (\rho) = \frac{OD_{specimen} - OD_{blank}}{OD_{standard} - OD_{blank}} \times 100\% \tag{9}$$

$OD_{specimen}$ was the absorbance value of the supernatant, $OD_{standard}$ was the absorbance value of the standard sample of BCA, and OD_{blank} was the absorbance value of the working solution.

2.7. Cell isolation and provenance

Bone marrow mesenchymal stem cells (MSCs) and osteoblasts (OBs) were extracted from the femur and cranial bone of male Sprague Dawley rats (SD; 1 month old; Dashuo biotech Chengdu, China), respectively. MC3T3-E1, 143b, MG-63, and UMR-106 were provided by iCell Bioscience Inc (Shanghai, China).

2.8. Extract preparation

2 g of sterilized powders (high-pressure steam sterilization, 120 °C, 2 h) were added to centrifuge tubes with 40 mL of α-MEM culture medium, and then put the centrifuge tubes in a thermostatic oscillator (90 rpm) for 7 d. When the release process was finished, the mixture was centrifuged (4000 rpm) for 2 min, and the supernatant was extracted for further bacterial filtration. 10% FBS and 1% penicillin/streptomycin were added to the above-mentioned supernatant to form an ion extract-contained α-MEM culture medium, and then the solution was well shaken and placed in a refrigerator at 4 °C for storage.

2.9. Cytocompatibility assessment

The prepared ion extract-contained α-MEM culture medium (mentioned in section 2.8) was cultured for osteoblast precursor cells (MC3T3-E1), and the cytocompatibility of the element-doped HA extract was evaluated. MC3T3-E1 cells were seeded in a 96-well plate at a concentration of 5000 cells/well, and cultured with 200 μL of α-MEM culture medium for 12 h until cells were adhered. Then the medium was discarded and the cells were rinsed twice with PBS solution. The ion extract-contained α-MEM culture medium was added to the wells and cultured at 37 °C in a humidified incubator with 5% CO_2 for 72 h. Subsequently, the cell activity of each group was tested by Alamar Blue reagent, and the absorbance values were detected at wavelengths of 570 nm and 600 nm using a microplate reader. Cell-free complete medium was used as a negative control, and MC3T3-E1 cells cultured in a complete medium were used as a positive control. The relative growth rate (RGR) of cells was calculated by formula (10):

$$RGR = \frac{\left[OD_{sample(570nm)} - OD_{sample(600nm)}\right] - \left[OD_{blank(570\ nm)} - OD_{blank(600\ nm)}\right]}{\left[OD_{complete(570nm)} - OD_{complete(600nm)}\right] - \left[OD_{blank(570nm)} - OD_{blank(600\ nm)}\right]} \times 100\% \tag{10}$$

Where $OD_{sample(570nm)}$ and $OD_{sample(600nm)}$ represented the optical absorption intensity values of the sample measured at the wavelength of 570 nm and 600 nm. $OD_{blank(570nm)}$ and $OD_{blank(600nm)}$ represented the optical absorption intensity values of the negative control group detected at 570 nm and 600 nm wavelength of the negative control group. $OD_{complete(570nm)}$ and $OD_{complete(600nm)}$ represented the optical absorption intensity values of the negative control group detected at wavelength of 570 nm and 600 nm. The experiment was repeated three times, and the mean value was calculated.

2.9.1. Cell viability assessment

0.4 g of the above-prepared and sterilized powders (high-pressure steam sterilization, 120 °C, 2 h) were added to centrifuge tubes with 40 mL of α-MEM culture medium, the other steps were the same as those in section 2.8. Subsequently, the prepared extracts were co-cultured with osteogenic precursor cells (MC3T3-E1) to evaluate the cell viability of the samples. MC3T3-E1 was seeded in a 48-well plate with 3×10^3 cells/well, and then incubated with the α-MEM complete medium until the cells were adherent. After the original medium was discarded, the cells were washed with PBS, and then the prepared element-doped HA extract medium was added and cultured for 7 d. Note that, the culture medium was changed every 48 h. CCK-8 reagent was used to detect cell proliferation at 3, 5, and 7 d. According to the steps specified by the manufacturer, the absorbance value was detected at the wavelength of 450 nm using a microplate reader. The proliferation status of MC3T3-E1 was calculated and analyzed by the following formula (11):

$$\text{Cell Proliferation} = \frac{OD_{contrast} - OD_{blank}}{OD_{experiment} - OD_{blank}} \times 100\% \tag{11}$$

Where $OD_{contrast}$ was the absorbance of the control group (cells cultured with basic medium), OD_{blank} was the absorbance of the blank group (only containing medium and CCK-8), and $OD_{experiment}$ is the absorbance of the experimental group (cells cultured with ion extract medium). The experiment was repeated three times, and the average value was retained for calculation.

2.9.2. Cell morphology assessment

The osteoblasts were seeded in a 48-well plate at a density of 3×10^3 cells/well. After the OBs were adherent to the walls, 10 mg/mL of element-doped HA ion extract medium was added to the culture medium and incubated for 5 d. The cells were fixed with cell fixing solution, and then the cells were permeated with 0.1%Triton X-100 for 5 min, and

then washed with PBS. Next, DAPI and rhodamine B staining solution were added successively and incubated at room temperature for 5 min and 7 min, respectively. After rinsing and washing, the cell morphology was observed and recorded by a fluorescence microscope.

2.10. Evaluation of osteogenic differentiation potentials in vitro

The osteogenic differentiation potentials of Se/Sr/Zn-HA were evaluated by detecting ALP activity and alizarin red staining. MSCs were seeded in a 48-well plate at a concentration of 10,000 cells/well. After the MSCs attachment, the α-MEM culture medium was replaced with certain amount of the corresponding ion-extract medium (10 mg/mL) containing osteogenic induction fluid. After 7 days and 14 days of culture, MSCs were gently rinsed with phosphate buffer (PBS) and lysed on ice with RIPA lysis buffer, and the liquid was collected and centrifuged at 1×10^4 rpm for 5 min. Afterwards, Alkaline Phosphatase Assay Kit was used to test the supernatant to detect the secretion of ALP activity according to the manufacturer's protocol. A microplate reader was used to detect the OD value (405 nm) and calculate the activity of ALP. The cytoskeleton and nucleus of MSCs were stained with Phalloidin-rhodamine and DAPI, respectively, to reveal cell morphology. In brief, after MSCs were cultured for 7 days, cell fixation solution was added, followed by adding 1% Triton X-100 to permeabilize the cells for 5 min, and then rinsed with PBS. Then rhodamine-labeled phalloidin staining solution was added and incubated for 30 min at room temperature under dark conditions. After rinsing with PBS, the cells were staining with DAPI for 5 min, and observed and recorded by a fluorescence microscope.

When MSCs was cultured for 14 d, total protein content from MSCs was isolated using radio immunoprecipitation assay (RIPA) lysis, and the protein concentrations were determined by the bicinchoninic acid (BCA) assay. Equal amounts of proteins were separated by sodium dodecyl sulfate (SDS)-polyacrylamide gel electrophoresis (PAGE) and transferred onto a pure nitrocellulose blotting membrane. Membranes were blocked with 5% (w/v) nonfat milk for 1 h at room temperature and incubated with primary antibodies, including those against COL I (1:1000, 66761-1-Ig, Proteintech), OCN (1:1000, 23418-1-AP, Proteintech), RUNX2 (1:500, ABclonal), and OPN (1:1000, 22952-1-AP, Proteintech) overnight at 4 °C. Then, the membranes were incubated with HRP-conjugated secondary antibody (anti-rabbit or anti-mouse) for 1 h. The blots were visualized through densitometry via Image J software and the ECL-Plus detection system (Santa Cruz Biotechnology, Santa Cruz, CA). All sample experiments were repeated three times, independently.

Total RNAs from MSCs were extracted through TRIzol extraction. Both the amount and purity of the RNA preparation were confirmed by measuring the absorbance ratio at 260/280 nm. The relative RNA expression level was evaluated by real-time quantitative polymerase chain reaction (qRT-PCR), and the housekeeping gene glyceraldehyde-3-phosphate dehydrogenase (GAPDH) was used as the loading control. All PCR amplifications were performed in a final reaction mixture (20.0 μL), and the relative primer sequences are listed in Table S1 (Supporting Information). The amplification reaction was performed using SYBR Green Master Mix (Yeason, 11201ES03, China) for 40 cycles, and relative expression was calculated according to the $2-\Delta\Delta Ct$ method. Each procedure was performed in triplicate independently to ensure minimal bias.

On day 21st, the BMSCs were washed thrice with PBS and fixed with 4% paraformaldehyde for 15 min. Then the fixative was discarded and the cells were washed with distilled water for three times. 0.25 mL of 0.2% alizarin red solution (Beyotime Biotechnology, Shanghai, China) was added and dyed for 20 min after a full adsorption of water. The dye was discarded and the cells were washed with distilled water for three times followed by adding an appropriate amount of distilled water to each hole to avoid hole drying. Finally, the samples were observed and photographed by a fluorescence microscope (CKX53, Olympus, Japan).

2.11. Antibacterial evaluation in vitro

1 mL of *Escherichia coli* solution (1×10^6 CFU/mL) and 10 mg of sterile element-doped HA were mixed thoroughly in an EP tube, then incubated in a bacterial incubator for 24 h. The co-culture of bacterial solution with the same mass of PBS was defined as a positive control. At the end of the culture, 100 μL of bacterial solution was put into a 96-well plate and the absorbance (wavelength = 450 nm) was detected by a microplate reader. The co-culture inhibition experiment of *Staphylococcus aureus* was carried out with the same experimental procedure. 80 μL of extract (10 mg/mL) and 20 μL of *Escherichia coli* solution (1×10^6 CFU/mL) were coated on the bacterial solid culture dishes in sequence, and then the dishes were sealed, inverted, and put into a bacterial incubator for 24 h. The bacterial solid culture dishes were coated with 80 μL of PBS and 20 μL of bacterial solution as positive controls and coated with 100 μL of PBS as a negative control. After cultivation, the growth of the colony was observed and photographed. The antibacterial test of *Staphylococcus aureus* was the same as above. The experiment was repeated three times.

2.12. Anti-tumor evaluation in vitro

Human osteosarcoma cells (143B and MG-63) and rat osteosarcoma cells (UMR-106) were co-cultured with the ion extract (10 mg/mL) of element-doped HA samples. The proliferation of 143B and MG-63 was detected by the CCK-8 kit, and the survival status of UMR-106 was examined by live/dead staining. Briefly, 143B, MG-63, and UMR-106 were seeded in 48-well plates at a concentration of 3×10^4 cells/well, and DMEM high glucose medium was added to culture cells. After the cells were adherent to the wall, the DMEM complete medium was replaced with the DMEM ion extract medium of each experimental group and cultured for 3 days. CCK-8 cell viability was detected at 1 day and 3 days, and live/dead staining was performed on day 3. Cell-free DMEM complete medium was used as the negative control, while 143B, MG-63, and UMR-106 cultured in DMEM high glucose complete medium were used as the positive control. CCK-8 detection procedure and cell viability calculation formula were the same as above, and the live/dead staining was performed following the vendor's instructions. The experiment was repeated three times.

2.13. Anti-tumor evaluation in vivo

The cultured and expanded 143B cells were inoculated subcutaneously in the hind legs of BALB/c nude mice (3–4 weeks, weighing about 15 g) with a cell number of 1×10^7/100 μL. All the procedures were performed in the Ninth People's Hospital Affiliated with Shanghai Jiao Tong University School of Medicine (S9H9-2019-A490-1). When the tumor grew to about 10 mm^3, the nude mice were treated with a peritumoral injection. Mice in the control group were injected with 0.2 mL of PBS, and mice in the experimental group were injected with 50 mg/mL of a mixture of saline and synthetic samples (100 μL/mice). Dosing was performed every three days, and the changes in mouse body weight and tumor volume were recorded. Animal experiments were divided into nine groups, with four animals in each group. The groups were the control group, HA, Se-HA, Sr-HA, Zn-HA, Se/Sr-HA, Se/Zn-HA, Sr/Zn-HA, and Se/Sr/Zn-HA. After 8 days, the tumor-bearing mice were sacrificed, and the heart, liver, spleen, lung, kidney, and tumor tissues were obtained, dehydrated, waxed, sectioned, and stained. The fresh organs were added to a 4% paraformaldehyde solution and soaked for 3 days for tissue fixation. The fixed tissue was rinsed under running water for 120 min and dehydrated in a gradient from low to high, and the tissue was finally placed in xylene. After dehydration, the samples were placed in a waxing machine for waxing and ultrathin sectioning. Sections were soaked in xylene, followed by soaked in ethanol, then treated with graded ethanol, and stained with hematoxylin/eosin finally. The tumor volume was calculated through formula (12):

$$\text{Tumor volume } (cm^3) = \frac{L_1 \times L_2^2}{2000} \quad (12)$$

Where L_1 represented the tumor length, L_2 represented the tumor width after treatment. The obtained samples were ready for testing, and the tumor inhibitory rate was calculated through formula (13):

$$\text{Tumor inhibitory rate } (100\%) = \frac{V_1 - V_2}{V_1} \times 100\% \quad (13)$$

Where V_1 represented the tumor volume before treatment and V_2 represented the tumor volume after treatment.

2.14. Evaluation of bone healing in a critically sized rat femoral defect in vivo

The animal surgical procedures involved in this study follow the recommendations of the Animal Care and Experiment Committee of Shanghai Ninth People's Hospital, Shanghai Jiao Tong University School of Medicine (SH9H-2021-A433-SB). In brief, 36 adult female SD rats (8 weeks old, weight: 225g–275g, Dashuo, Chengdu) were divided into 6 groups and anesthetized by intraperitoneal injection of 4% pentobarbital sodium (0.9 mL/100 g). A hole with a diameter of 3 mm and a depth of 1 mm was subsequently drilled in the lateral epicondyle using a minimally invasive method using a hand drill. HA-PCLs, Se-HA-PCLs, Sr-HA-PCLs, Zn-HA-PCLs, and Se/Sr/Zn-HA-PCLs were implanted into the constructed hole, and the non-implanted hole was set as the

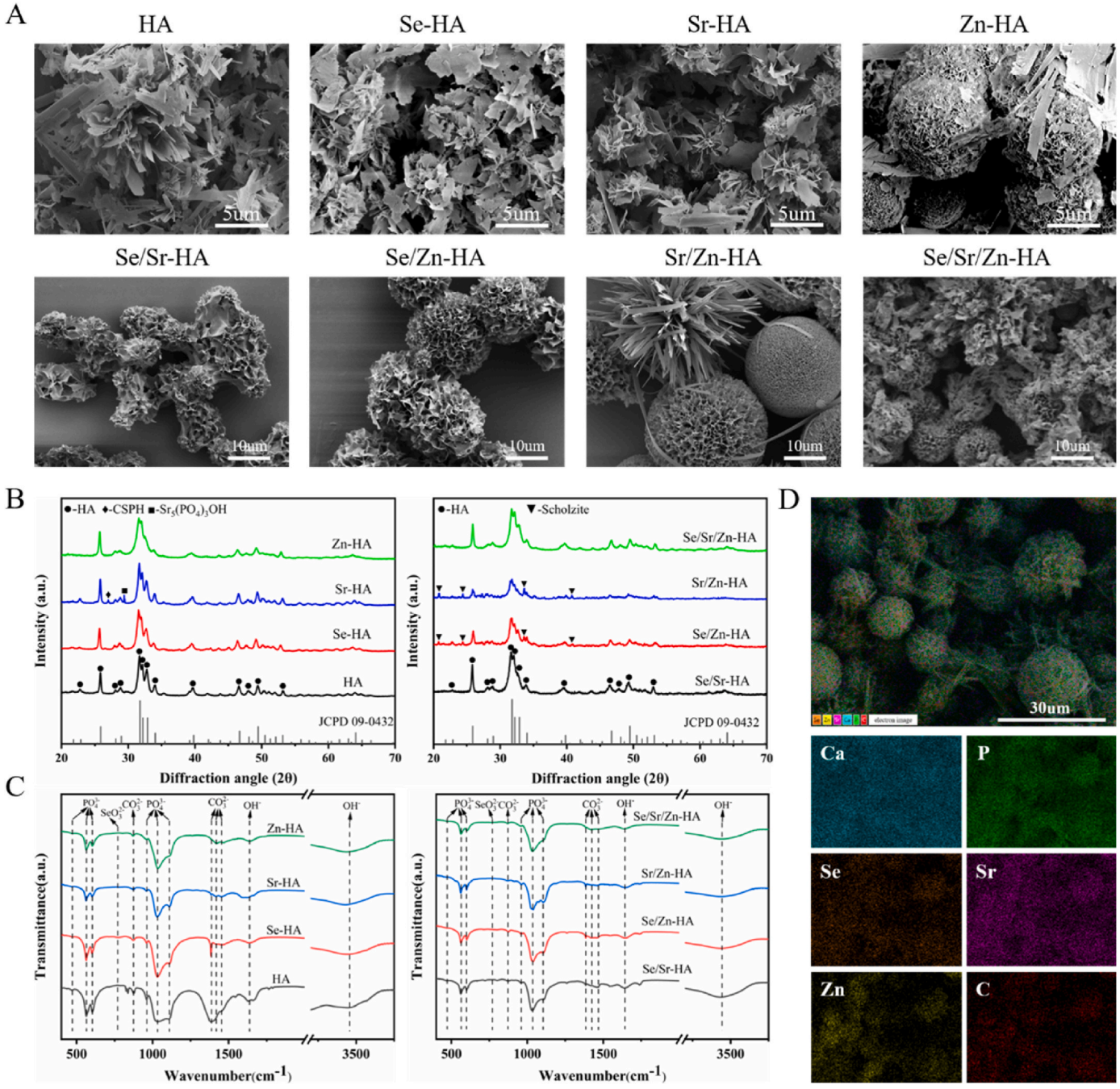

Fig. 2. Characterization of HA, Se-HA, Sr-HA, Zn-HA, Se/Sr-HA, Se/Zn-HA, Sr/Zn-HA, and Se/Sr/Zn-HA. (A) SEM images, (B) XRD patterns, (C) FTIR spectra, and (D) Element mapping of Se/Sr/Zn-HA.

control group. The wound was carefully sutured after implantation. After surgery, the rats were injected with penicillin (4×10^5 units) daily to prevent wound infection for one week. Among them, 18 SD rats were sacrificed by intraperitoneal injection with an overdose of pentobarbital sodium on week 4, the remaining 18 rats were sacrificed on week 12, and the femurs were removed for further characterization.

2.15. Statistical analysis

All data were expressed as mean ± SD (standard deviation). The difference among groups were determined by one-way analysis of variance (ANOVA) and Tukey multiple comparison test, when $p < 0.05$ (* means $p < 0.05$, ** means $p < 0.01$, *** means $p < 0.001$, **** means $p < 0.0001$) was considered to be statistically significant.

3. Results and discussion

3.1. Fabrication and characterization of HA and the element-doped HA

In this study, the HA and element doped HA were synthesized by hydrothermal method, which was attributed to the low reaction temperature, good crystallinity of products, and easy control of product morphology, and provided the possibility to obtain sub-micron or even nano-scale or nano-structured materials [35]. Urea was used as a precipitator in the reaction system. Urea gradually decomposed to produce NH_3 and CO_2 under hydrothermal conditions, which enhanced the pH of the solution and promoted the formation and growth of HA crystals [36]. In addition, the production of CO_2 was conducive to the formation of carbonate-HA, which was similar to the composition of human bone [37]. SEM results showed that the pure HA assumed a banded crystal shape (Fig. 2A) with a length of 2–10 μm and a width of 1 μm, which were consistent with the previous experimental results under the same reaction conditions (150 °C, 3 h) [38–41]. Se-HA facilitated nano-flake and flake aggregation, and the length was shortened to be 2–5 μm while the width increased variably. There was also a spherical structure composed of a few sheets, which was consistent with our previous research findings [42]. Sr-HA showed a more regular aggregate shape compared with Se-HA, while the particles had a radial petal-like structure. The average width of the particles was approximately 5 μm, and there were few incomplete microspheres, indicating that Sr-HA continued to change from a radial petal-like structure to a spherical structure with increasing doping. The morphology of the Zn-HA particle was relatively uniform, which consisted of a stack of nano-flakes forming a complete micro-spherical structure with a diameter of approximately 7–9 μm, meanwhile, it can be regarded as a micro/nanocrystal structure [41]. The Zn-HA microspheres were connected and had similar sizes, indicating that a 15% molar concentration of Zn doping can induce a uniform surface morphology for HA. Se/Sr-HA was a ball-like junction structure comprising a stack of flakes, the ball-like structure was radial and similar to that of Sr-HA. Se/Zn-HA was assumed to be a relatively regular spherical structure, but its sphericity was not as good as that of Zn-HA. The flakes of Se/Zn-HA were relatively sparse, with diameters of 15–25 μm, which were larger than those of Zn-HA, indicating a structural regulation caused by both Zn^{2+} and SeO_3^{2-}. Sr/Zn-HA displayed a regular spherical structure with sparse and radial flakes, and some of Sr/Zn-HA were denser than Zn-HA, with diameters of 20–30 μm, which were larger than those of Zn-HA, indicating that Sr^{2+} and Zn^{2+} synergistically regulated the structure of Sr/Zn-HA. The morphology of Se/Sr/Zn-HA particles was different from that of the single-element doped HA particles. The diameters of the Se/Sr/Zn-HA ranged from 2 to 10 μm, the morphologies of which composed of radial petal-like and microspheres. The radial petal-like structure was similar with the structure of Sr-HA, and the microsphere-like structure was consistent with the structure of Zn-HA. Meanwhile, there were more microspheres in Se/Sr/Zn-HA compared to Zn-HA, and the particles of Se/Sr/Zn-HA were connected to each other. The morphology of Se/Sr/Zn-HA was similar to the combined morphology of the single-element doped hydroxyapatite Se-HA, Sr-HA, or Zn-HA, but the proportion of flakes was slightly different. HA with a unique micro/nano morphology could be prepared via hydrothermal synthesis using different elements and doping magnitudes, which was different from the double-element doped HA with a nanorod shape prepared by sol-gel method or a spherical shape prepared by co-precipitation method [43,44].

The phase of the element-doped HA was analyzed using XRD to explore the effects of element doping on the growth direction, crystallinity, and lattice parameters of the HA crystal. The results showed that the pattern of the prepared HA sample was similar to the HA standard map (JCPDS09-0432) [45]. The patterns of other doped samples also presented the characteristic peak of HA, and the element-doped HA samples maintained the main phase of HA (Fig. 2B). A small amount of $Ca_9Sr(PO_4)_6(OH)_2$ (CSPH) and $Sr_5(PO_4)_3OH$ existed in Sr-HA, which was attributed to the reaction of Ca^{2+}, Sr^{2+}, PO_4^{3-}, and OH^-. Note that the number of OH^- gradually increased with the decomposition of urea to produce NH_3 and CO_2 during the reaction. As demonstrated, CSPH and $Sr_5(PO_4)_3OH$ possessed excellent osteoinductivity, which improved the biological activity of Sr-HA [46,47]. Se/Zn-HA and Sr/Zn-HA contained a small amount of scholzite [$Ca_2Zn(PO_4)_2{\bullet}2H_2O$], which may be attributed to the reaction system changed from acid to neutral as less urea decomposition in the initial stage of reaction, resulting in the formation of scholzite. Liu et al. have confirmed that scholzite displayed excellent biocompatibility and induced the expression of osteoblast-related proteins [48]. The results demonstrated that the basic phase of HA did not change with low doping content (<15%) irrespective of single- or multi-element co-doping. The peak ratio of (300)/(211) of pure HA (the crystal plane position was shown in Table S2) was higher than that of the standard card, which indicated that the crystal lattice grew preferentially along the c-axis direction under hydrothermal conditions to form a filamentous or banded morphology. Compared with pure HA, the (300)/(211) peak intensity ratios of element-doped HA gradually decreased, indicating that the growth of the crystal on the plane was slowed down with an increase of element doping content. The tendency of preferential growth on the c-axis was also weakened, and the crystal was transformed from a long sheet to a short and wide sheet. The peak intensity ratio of (002)/(300) was also changed, indicating that the element doping changed the growth direction of the HA crystal and the character transformation of its morphology. Therefore, the morphology of HA could be manipulated by adding urea and adjusting the element doping amount to achieve a specific purpose. The characteristic diffraction peak of the Se/Sr/Zn-HA particles slightly shifted to the left with a lower-angle turn, which was consistent with previous studies that ion substitution could slightly shift the characteristic peak [49,50]. Moreover, higher content of element doping led to a stronger shift of the diffraction peaks of the element-doped HA. The sharpness of the diffraction peaks of the samples decreased to varying degrees after elements doping, and the increment of doping content would reduce the crystallinity of the samples, but not affect the stability of the crystal, as shown in Table S3. The grain size of HA was 53 nm, and the grain size growth of Se-HA, Sr-HA, and Zn-HA was related to the ionic radius or group radius of the doped elements [46]. In the process of replacement of Ca^{2+} by other elements, the grain size of Sr-HA was larger than that of Zn-HA because the radius of Sr^{2+} was larger than that of Zn^{2+}. As for Se-HA, the smallest grain size may be attributed to the least doping amount. The grain size of Se/Sr/Zn-HA was between Se-HA and Sr-HA, which was accorded with the substitution theory of doping ion radius [51]. The cell volume has nothing to do with the type and amount of element doping, remaining at 530 AI.

FTIR was used to analyze the chemical structure of the doped HA. Fig. 2C displayed the functional group absorption peak of HA in the FTIR spectra of all samples. The broad peak in the range of 3700–2500 cm^{-1} was the H–O tensile vibration peak of H_2O molecules adsorbed on the sample surface, and the peak at 1639 cm^{-1} was the H–O bending vibration peak of molecules. The spectrums for the sample showed the

characteristic peak of the H_2O molecule, however, the intensity was weak, indicating that part of the adsorbed water was removed by drying during the sample preparation. The C–O characteristic peaks of CO_3^{2-} appeared at 872 cm^{-1} and 1453 cm^{-1}, indicating the presence of CO_3^{2-} in the doped sample and type A and type B substitutions to form a small amount of carbonate apatite [52]. The CO_3^{2-} substitution did not affect the biological function of the sample. Instead, previous studies had shown that the combination of carbonate apatite and hydroxyapatite was more biocompatible than pure HA because human bone contained carbonate apatite [53]. The bending vibration peaks of the P–O bond in PO_4^{3-} appeared at 564 cm^{-1} and 602 cm^{-1}, and the tensile vibration peaks were located at 958 cm^{-1}, 1034 cm^{-1}, and 1108 cm^{-1} [54]. The results showed that element doping did not change the characteristic functional groups of HA, and only a small amount of carbonate apatite was generated during the synthesis. The EDS mapping of the selected surface (Fig. 2D) showed that Zn, Sr, and Se were uniformly distributed on the surface of Se/Sr/Zn-HA, which indicated that hydrothermal synthesis was successful for preparing Se, Sr, and Zn co-doped HA, and the sample contained a combination of crystal structures.

The valence states and forms of the doped elements in Se-HA, Sr-HA, Zn-HA, and Se/Sr/Zn-HA were detected by XPS. All the doped HA samples contained Ca, P, and O elements, and the C element in CO_3^{2-} during the synthesis (Fig. 3A) was consistent with the XRD results. In addition, Na_2HPO_4 was used as a phosphorus source, and a few characteristic Na 1-s peaks were observed for all the samples. Se-HA contained a Se-3D-characteristic peak at a binding energy of 65 eV, which was confirmed by the EDS results, indicating SeO_3^{2-} had been incorporated into the HA lattice successfully in this study. The Sr-HA sample demonstrated the characteristic peak of Sr 3p on the pattern, while the Zn-HA sample showed two peaks at the binding energies of 1022 eV and 1045 eV, which were characteristic peaks for Zn 2p 3/2 and 2p 1/2 of Zn–O [55,56]. At the above corresponding binding energy positions mentioned above, the Sr–O and Zn–O bonds were observed in the Sr-HA and Zn-HA samples, which belonged to the binding energy of CSPH and scholzite, respectively. The XPS spectra of Se/Sr/Zn-HA demonstrated the characteristic peaks of Se, Sr, and Zn at the same time, which was consistent with the results of the EDS mapping. The peak positions and valence states were also the same as those for single-element doping, which indicated that Se/Sr/Zn-HA contained the expected doping elements, and they did not affect each other and were stable in the HA

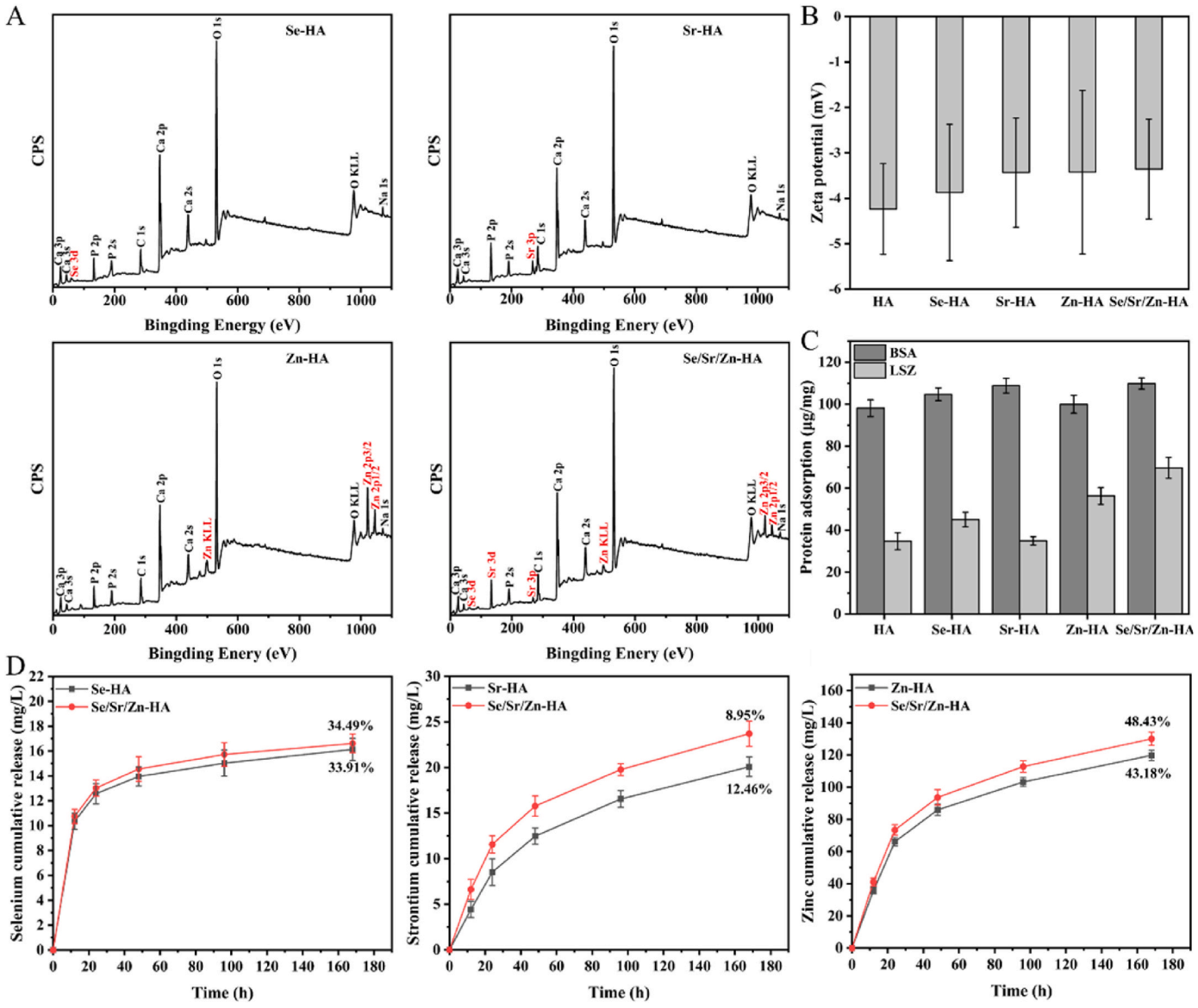

Fig. 3. Chemical valence, potential, protein adsorption capacity, and ion release of HA, Se-HA, Sr-HA, Zn-HA, and Se/Sr/Zn-HA. (A) XPS pattern, (B) Zeta potential, (C) protein adsorption, and (D) ion release curve. (n = 3).

lattice. The zeta potential of the samples in a physiological environment that mimics the human body at pH of 7.4 was shown in Fig. 3B (n = 3). The HA possessed the lowest potential of −4.2 mV among all the samples. The potential difference between the single-element doped HA and Se/Sr/Zn-HA was minimal at approximately −3.8 mV, indicating that the element doping had no significant effect on the electrical properties of the samples.

The most commonly used model proteins, BSA protein, and LSZ lysozyme were adopted to study the adsorption patterns of acidic and basic proteins on HA samples [57]. The BCA kit was used to detect the effects of the adsorption of the BSA protein and LSZ lysozyme on HA, Se-HA, Sr-HA, Zn-HA, and Se/Sr/Zn-HA. The amount of adsorbed protein (AP) was calculated by formula (8), and the adsorption effect of samples on BSA was shown in Fig. 3C (n = 3). About 100 μg of protein could be adsorbed on the surface of 1 mg of the sample. The protein adsorption by the materials was influenced by the surface charge, morphology, and specific surface area. The zeta potential showed no significant differences between the surface charges of the element-doped HA samples, and there were no significant differences in the BSA protein adsorptions. However, Se/Sr/Zn-HA showed a slightly higher BSA protein adsorption, which was similar to that of Sr-HA. Qi et al. have confirmed that the petal-like surface morphology has a lifting effect on protein adsorption [58]. The Se/Sr/Zn-HA adsorption of the LSZ lysozyme was significantly higher than those of HA and Sr-HA, which indicated that LSZ lysozyme adsorption mainly depended on the morphology of the Se/Sr/Zn-HA and Zn-HA rather than the surface charge. The spherical morphology of Se/Sr/Zn-HA and Zn-HA facilitated the adsorption of the LSZ lysozyme. The above results confirmed that Se/Sr/Zn-HA demonstrated the best protein adsorption due to its special surface morphology.

According to the cumulative release curve of elements (Fig. 3D) in the simulated *in vitro* environment, the element-doped HA samples rapidly released the doped element ions within the first 24 h, which gradually decreased within 72 h and finally stabilized in 168 h (n = 3). SeO_3^{2-} presented a fast release from Se/Sr/Zn-HA during the first 12 h, however, it reached a balance on the seventh day, and the release amount reached 34.49% of the actual doping amount. The release curve of Se-HA was similar to that of Se/Sr/Zn-HA, but the cumulative release amount and release percentage (33.91%) of Se-HA within 7 days were lower than those of Se/Sr/Zn-HA. The release trends of Sr^{2+} and Zn^{2+} still proceeded after 168 h of immersion, indicating that Sr^{2+} and Zn^{2+} could be continuously released in Se/Sr/Zn-HA samples. The cumulative Sr^{2+} release of Se/Sr/Zn-HA was higher than that of Sr-HA, but the release percentage was lower than that of Sr-HA by 12.46%. However, the cumulative release of Zn^{2+} was very high, which could reach half of the actual doping amounts (43.18% and 48.42%) in both Zn-HA and Se/Sr/Zn-HA. The release of Zn^{2+} was faster than that of Sr^{2+}, in line with that, more Zn^{2+} than Sr^{2+} was released. These were attributed to the larger ionic radius of Sr^{2+} than that of Zn^{2+} and the more stable replacement of Ca^{2+} in the Se/Sr/Zn-HA lattice [59]. The release curves for each element of Se/Sr/Zn-HA verified that the cumulative ion release of SeO_3^{2-}, Sr^{2+}, and Zn^{2+} co-doping was higher than that of the control group with single-element doping, which may be ascribed to the fact that the structure of Se/Sr/Zn-HA with a high specific surface area was more conducive to ion release. With the increase in the types and proportions of doping elements, the crystal structure of HA was imperfect, resulting in a more rapid dissolution of the samples [60]. Combined with the actual element doping results detected by XRF (Table 1), Se/Sr/Zn-HA possessed a higher actual element doping rate than Se-HA, Sr-HA, and Zn-HA, while releasing more functional ions in a neutral environment.

3.2. Evaluation of the antibacterial activities of HA and element-doped HA

Staphylococcus aureus and *Escherichia coli* were selected to represent Gram-positive and Gram-negative bacteria, respectively, and used to evaluate the antibacterial effect of element-doped HA [61]. The antibacterial activities of the extracts of HA, Se-HA, Sr-HA, Zn-HA, and Se/Sr/Zn-HA were quantitatively analyzed, and the viabilities of the bacteria after co-culturing them with the bacterial broth were shown in Fig. 4A and B (n = 3). The above results demonstrated that the viabilities of the bacteria exposed to HA and Se-HA were similar but slightly lower than those of the control group, indicating that the Ca^{2+} and PO_4^{2-} dissolved from the HA samples exerted little inhibitory effect on the bacteria, and SeO_3^{2-} dissolved from Se-HA samples possessed a slight effect on the bacteria compared to Ca^{2+} and PO_4^{2-}. Muhammad et al. had demonstrated that Se-HA displayed a better inhibitory effect on *E. coli* and *S. aureus* compared to HA, which was in accordance with the results of this study [62]. The extract of Sr-HA and Zn-HA displayed a better antibacterial effect than those of Se-HA and the control group, especially the Zn-HA, which was related to the excellent antibacterial function of Zn^{2+}. Wang et al. had confirmed that Zn-HA displayed a better antibacterial effect than Sr-HA and HA [63]. Although the antibacterial effects of Sr-HA, Zn-HA, and Se/Sr/Zn-HA were significantly different from those of the control group, Se/Sr/Zn-HA possessed the best antibacterial effect in the above extracts, whether co-cultured with *E. coli* or *S. aureus*, which indicated that the combination of the SeO_3^{2-}, Sr^{2+}, and Zn^{2+} exhibited better antibacterial activity. To intuitively illustrate the antibacterial effect of SeO_3^{2-}, Sr^{2+}, and Zn^{2+}, the sample extract above and the bacterial solution were used to inoculate to the solid medium and were cultured for 24 h to observe the growth of colonies. The growth of *E. coli* was shown in Fig. 4D. The colony density of HA, Se-HA, and Sr-HA was similar and slightly lower than that of the control group. However, the colony density of the Zn-HA was fewer than HA, Se-HA, and Sr-HA, indicating that the inhibitory effect of Zn^{2+} was more obvious, which was consistent with the results of other studies [45,64]. As expected, the colonies of Se/Sr/Zn-HA were the lowest among all the groups after a 24-h culture with *E. coli*-coated plates, with only a few sporadic colonies, which was attributed to the synergistic antibacterial function of SeO_3^{2-}, Sr^{2+}, and Zn^{2+}. As revealed in Fig. 4C, the colony densities of HA, Se-HA, Sr-HA, and Zn-HA were similar but slightly lower than that of the control group. The inhibitory effect on *S. aureus* was less pronounced than that of *E. coli* due to the bacterial membranes of Gram-positive and -negative bacteria containing different structures, it was more difficult for ions to penetrate the membrane of *S. aureus*, which was confirmed by the reports of previous studies [65,66]. Although the colony density of *S. aureus* in Se/Sr/Zn-HA was higher than that of *E. coli*, Se/Sr/Zn-HA still displayed the superior antibacterial effect, indicating that SeO_3^{2-}, Sr^{2+}, and Zn^{2+} combined administration could obtain the best antibacterial effect. The above results indicated that Se/Sr/Zn-HA possessed the best antibacterial effect on both *S. aureus* and *E. coli*, which confirmed the antibacterial advantage of the SeO_3^{2-}, Sr^{2+}, and Zn^{2+} in synergistic administration.

Table 1
Theoretical doping efficiency (χ_{t-O}) and actual doping efficiency ($\chi_{\alpha-O}$) of samples determined using XRF.

Sample	χ_{t-Se}(%)	χ_{t-Sr}(%)	χ_{t-Zn}(%)	$\chi_{\alpha-Se}$(%)	$\chi_{\alpha-Sr}$(%)	$\chi_{\alpha-Zn}$(%)
Se-HA	5	–	–	2.32	–	–
Sr-HA	–	10	–	–	4.61	–
Zn-HA	–	–	15	–	–	9.21
Se/Sr-HA	5	10	–	2.86	6.47	–
Se/Zn-HA	5	–	15	3.99	–	11.47
Sr/Zn-HA	–	10	15	–	8.17	11.97
Se/Sr/Zn-HA	5	10	15	2.50	7.24	9.96

3.3. Evaluation of the biocompatibilities of HA and the element-doped HA

In this study, the proliferation of MC3T3-E1 and OBs was used to evaluate the biocompatibility of the HA, Se-HA, Sr-HA, Zn-HA, and Se/

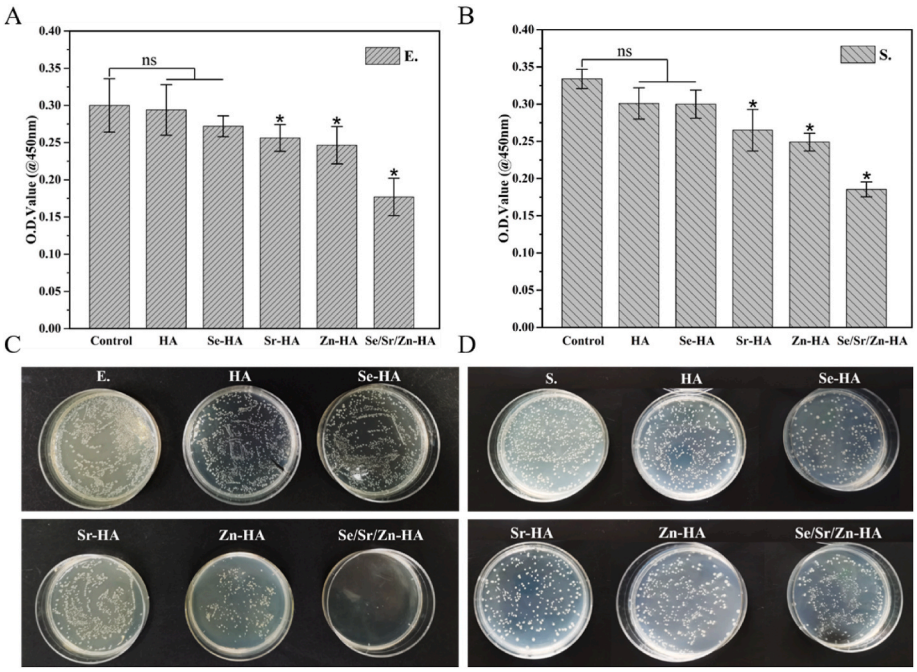

Fig. 4. Evaluation of the antibacterial properties of HA, Se-HA, Sr-HA, Zn-HA, and Se/Sr/Zn-HA ion extract co-cultured with bacteria for 24 h. (A) The OD value of the ion extract after co-culture with *E. coli*. (B) The OD value of ion extract after co-culture with *S. aureus*. (C) Co-coating plate of *E. coli* and ion extract. (D) Co-coating plate of *S. aureus* and ion extract. (n = 3, *p < 0.05.)

Sr/Zn-HA. The proliferation of MC3T3-E1 was shown in Fig. 5A. MC3T3-E1 increased gradually with the extension of culture time, the number of MC3T3-E1 in the experimental group was higher than those of the control group at each time point (n = 3). The growth rate of MC3T3-E1 was approximately logarithmic, which was consistent with the growth rate of normal cells, indicating that the ions released from the samples

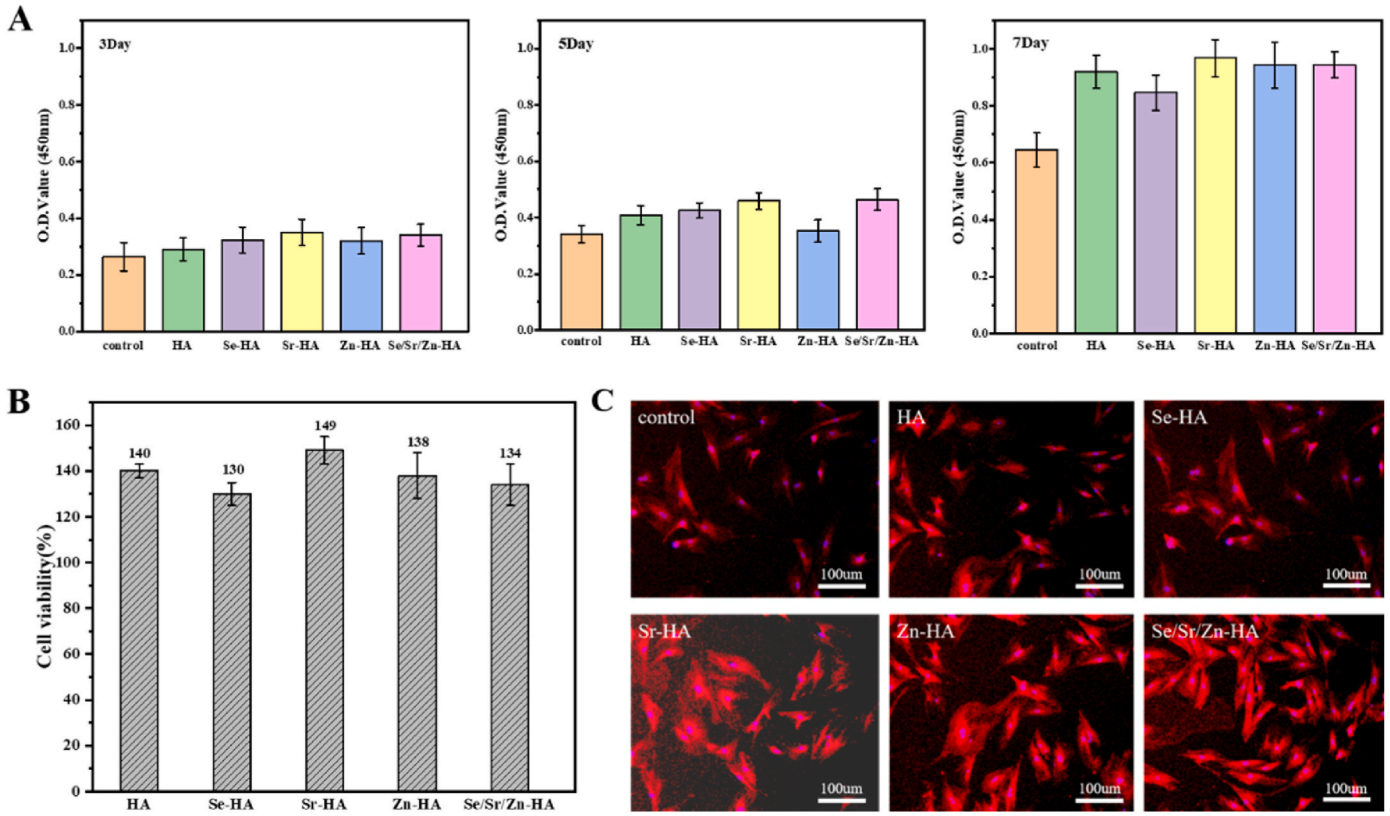

Fig. 5. Evaluation of the biocompatibilities of HA, Se-HA, Sr-HA, Zn-HA, and Se/Sr/Zn-HA *in vitro*. (A) The proliferation of MC3T3-E1 co-cultured with the ion extract for 3, 5, and 7 days. (B) The activities of cells of the ion extract co-cultured with MC3T3-E1 for 3 days. (C) The morphology of cells of OBs co-cultured with the ion extract for 5 days. (n = 3).

possessed excellent biocompatibility. After 3 days of culture, the MC3T3-E1 viabilities of Se-HA, Sr-HA, Zn-HA, and Se/Sr/Zn-HA were similar, which indicated that SeO_3^{2-}, Sr^{2+}, and Zn^{2+} released from the samples had no obvious effects on cell growth during the early stages of cell culture. After 5 days of culture, the number of MC3T3-E1 in the Zn-HA was less than that of the other experimental groups, and the Zn^{2+} in the extract slowed down the proliferation of MC3T3-E1, which was consistent with the report of a previous study [67]. The MC3T3-E1 exhibited a good growth tendency in Se-HA, Sr-HA, and Se/Sr/Zn-HA. The extract of Se/Sr/Zn-HA contained SeO_3^{2-}, Sr^{2+}, and Zn^{2+}, and the inhibitory effect of Zn^{2+} on cells was reduced, therefore, the cells showed good viability and proliferation. After 7 days of culture, the cells cultured with the element-doped HA showed slightly greater proliferation than those cultured with Se-HA, which may be attributed to the high concentration of SeO_3^{2-} which can effectively kill tumor cells while inhibiting the proliferation of osteoblasts [68]. The effect of Se/Sr/Zn-HA was similar to those of Sr-HA and Zn-HA, indicating that the synergistic administration of the SeO_3^{2-}, Sr^{2+}, and Zn^{2+} can facilitate a stable proliferation of MC3T3-E1 after prolonged culture. In addition, Se/Sr-doped HA has no adverse effect on the activity of MSCs compared to Se-doped HA or Sr-doped HA [69]. Wang et al. have confirmed that the osteogenic properties of Zn/Sr-codoped HA were better than Zn-doped HA or Sr-doped HA [63]. These results demonstrated that the extracts of HA, Se-HA, Sr-HA, Zn-HA, and Se/Sr/Zn-HA revealed good biocompatibility with MC3T3-E1. When the concentration of the extracts was increased from 10 to 50 mg/mL, the viability of MC3T3-E1 after the 72-h culture was shown in Fig. 5B (n = 3). All the experimental groups affected the proliferation of MC3T3-E1 without cytotoxicity, and the cell viability was higher than 100%. However, Se-HA was associated with the lowest cell growth rate. Previous studies have shown that a certain amount of Se can affect the proliferation of normal cells [42,70,71]. Se-HA decreased the cell proliferation rate but did not show cytotoxicity compared to the control group. The Sr-HA exerted the best effect on MC3T3-E1 proliferation, indicating that Sr^{2+} can significantly improve the viability of bone cells. The addition of Sr^{2+} can increase the solubility of Sr-HA, and the release of Sr^{2+} can promote the proliferation of MC3T3-E1 [72]. The viabilities of MC3T3-E1 cultured with the Zn-HA and HA extracts were similar, indicating that Zn^{2+} exerted no adverse effect on the cell viability of HA. The cell RGR of the Se/Sr/Zn-HA group was 134%, which was between Sr-HA (149%) and Se-HA (130%) groups because the pro-proliferation effect of the Sr^{2+} compensated for the negative effect of SeO_3^{2-}, therefore, the Se/Sr/Zn-HA showed good cell compatibility even at higher concentrations [62]. The concentration of the sample extract adopted in subsequent cell experiments was lower than 50 mg/mL, and the corresponding cytotoxicity test was no longer performed. To further investigate the effect of the sample extracts on cell proliferation, OBs cultured for 5 days with the ion extracts (10 mg/mL) were stained with DAPI and rhodamine B, as shown in Fig. 5C. The OBs demonstrated good adhesion and spread on the culture of the sample extracts, they were spindle-shaped and had several pseudopodia. Many studies have demonstrated that HA modified with SeO_3^{2-}, Sr^{2+}, or Zn^{2+} can effectively enhance its biological activity and promote the proliferation and differentiation of OBs [33,73,74]. These results indicated that the element-doped HA extracts demonstrated good cell viability and generated no cytotoxic effects on OBs. The number of cells that were spread, indicated that the ion extracts of HA, Se-HA, Sr-HA, Zn-HA, and Se/Sr/Zn-HA showed good proliferative effects on OBs.

3.4. *Evaluation of the osteogenic differentiation potentials of HA and element-doped HA in vitro*

The ability to induce osteogenic differentiation was evaluated by determining the ALP activity and alizarin red staining of rat bone marrow mesenchymal stem cells (BMSCs) cultured with extracts of samples. Fig. 6A showed that the ALP activity of BMSCs cultured in the experimental and control groups (DMEM complete medium) increased steadily with the prolongation of the culture, confirming that the BMSCs grew optimally (n = 3). After 7 days of culture, the element-doped HA extracts exerted little effect on ALP activity compared to the control group, but the BMSCs displayed a tendency to differentiate into osteoblasts. After 14 days of culture, the ALP activity of the HA was enhanced relative to that of the control group, and the osteogenic differentiation was observed.

The levels of ALP secretion in BMSCs treated with Se-HA, Sr-HA, and Se/Sr/Zn-HA were significantly higher than those of the control group after 14 days. Relevant studies have confirmed that Se or Sr-doped HA can increase the expression of ALP in MSCs compared to pure HA [75,76]. Zn-HA has a minimal effect on the differentiation of BMSCs, and the results after 7 and 14 days of culture were a little higher than those of the

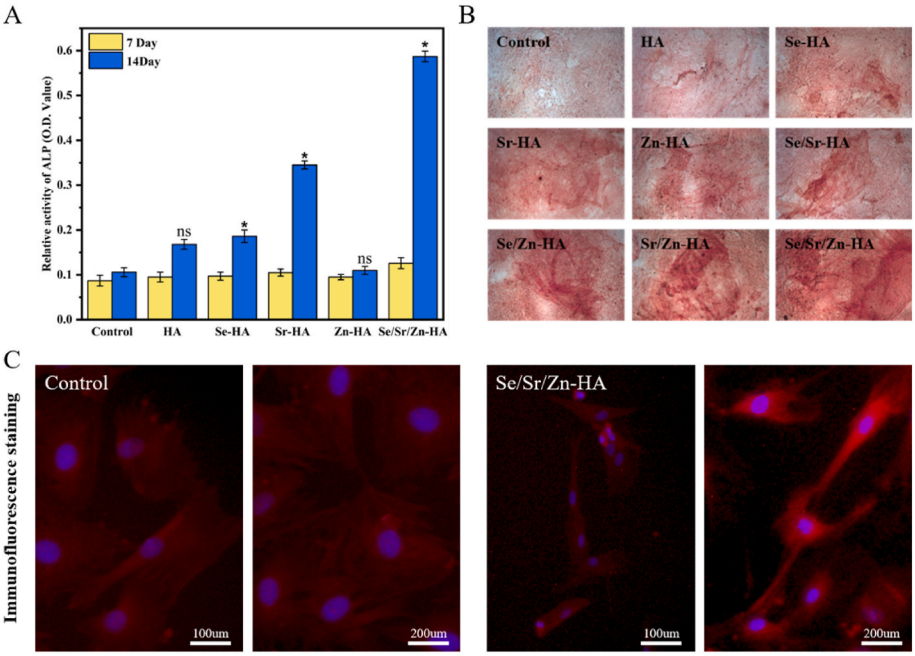

Fig. 6. Evaluation of the osteogenic differentiation potentials of HA, Se-HA, Sr-HA, Zn-HA, and Se/Sr/Zn-HA. (A) Levels of ALP secretion by BMSCs after 7 and 14 days of culture with HA, Se-HA, Sr-HA, Zn-HA, and Se/Sr/Zn-HA. (B) ARS staining of BMSCs after 21 days of culture with α-MEM culture medium, HA, Se-HA, Sr-HA, Zn-HA, Se/Sr-HA, Se/Zn-HA, Sr/Zn-HA and Se/Sr/Zn-HA. (C) Rhodamine-labeled phalloidin and DAPI immunofluorescence staining of BMSCs after 7 days of culture with α-MEM culture medium and Se/Sr/Zn-HA. (n = 3, *p < 0.05.)

control group, which may be attributed to the higher Zn^{2+} concentration [77]. The ALP activity of Se/Sr/Zn-HA was the highest, which was approximately 3–4 times higher than that of the control group, indicating that SeO_3^{2-}, Sr^{2+}, and Zn^{2+} collaboratively promote the osteogenic differentiation of BMSCs. Combined with the results of the Se-HA, Sr-HA, Zn-HA, and HA, the Ca^{2+}, PO_4^{3-}, and CO_3^{2-} dissolved from HA also promoted the osteogenic differentiation of BMSCs as well, whereas SeO_3^{2-} or Sr^{2+} enhanced the proliferation and differentiation of BMSCs. It has been proved that both Se-HA and Sr-HA could promote the proliferation and differentiation of MSCs [78,79]. Se/Sr/Zn-HA contained the above ions, which can promote the proliferation and differentiation of BMSCs (Zn^{2+} had no obvious effect), therefore, it presented a good potential for promoting bone differentiation. The result of alizarin red staining was generally similar with that of ALP activity, however, Zn-HA promoted more calcium deposition than the control group, HA, and Se-HA, as shown in Fig. 6B. Previous studies have shown that Zn-HA has a more significant calcareous deposition effect than HA [80]. Compared with the control group, the material group had an obvious effect of calcareous deposition. Furthermore, with the increase of element type, the effect of calcareous deposition became more obvious. The results of alizarin red staining showed that SeO_3^{2-}, Sr^{2+}, and Zn^{2+} could promote osteogenic differentiation of MSCs, and the combination of SeO_3^{2-}, Sr^{2+}, and Zn^{2+} could achieve the best effect of osteogenic differentiation. Rhodamine-labeled phalloidin and DAPI immunofluorescence staining revealed that BMSCs assumed a polyangular star shape and spread without differentiation (Fig. 6C), indicating that BMSCs did not show morphological changes after 7 days of culture. For Se/Sr/Zn-HA, the morphology of the BMSCs changed significantly, the aspect ratio of the cells increased, and the cell pseudopodia extended to form a stretched structure, which was attributed to the synergistic administration of SeO_3^{2-}, Sr^{2+}, and Zn^{2+}. Relevant studies have confirmed that SeO_3^{2-}, Sr^{2+}, and Zn^{2+} can induce the proliferation and the expression of osteoblast-related proteins of MSCs, and accelerate osteogenic differentiation ultimately [81–83]. To compare the osteogenic differentiation potential of Se/Sr/Zn-HA and double-element doped HA, the expressions of osteogenic-related genes and osteogenic-related proteins were detected by RT-PCR and Western blot (WB) method, respectively, as shown in Fig. S2. The expressions of ALP, RUNX2, and COL I (except OPN) in BMSCs treated with Se/Sr/Zn-HA were higher than that of the double-element doped HA and the control group. Although the expression of OCN in double-element doped HA and Se/Sr/Zn-HA was similar, it was higher than that of the control group. The results of WB displayed that the expression levels of RUNX2, OCN, and COL I in the Se/Sr/Zn-HA g were higher than those of double-element doped HA and the control group, while the expression level of OPN was similar. Related studies have shown that SeO_3^{2-}, Sr^{2+}, and Zn^{2+} can promote osteogenic differentiation of MSCs, and the synergistic administration of the two ions could achieve a more significant osteogenic differentiation effect [25,33,82]. Considering the above results, it was reasonable to conclude that synergistic administration of the SeO_3^{2-}, Sr^{2+}, and Zn^{2+} achieved an enhanced osteogenic differentiation effect compared to the double-element doped HA and control group.

3.5. *Evaluation of the anti-tumor potential of HA and element-doped HA in vitro*

To fully verify the anti-tumor properties of element-doped HA, three types of osteosarcoma cells, 143b, MG-63, and UMR-106 (rat osteosarcoma cells) were cultured with the element-doped HA extracts. The extracts containing SeO_3^{2-} had the least of 143b, which was significantly different from the amount of other groups, indicating that SeO_3^{2-} possessed better anti-tumor effects, as shown in Fig. 7A (n = 3). Li et al. had demonstrated that Se-doped HA can promote ROS-mediated autophagy and apoptosis of osteosarcoma cells [32]. After 3 days of culture,

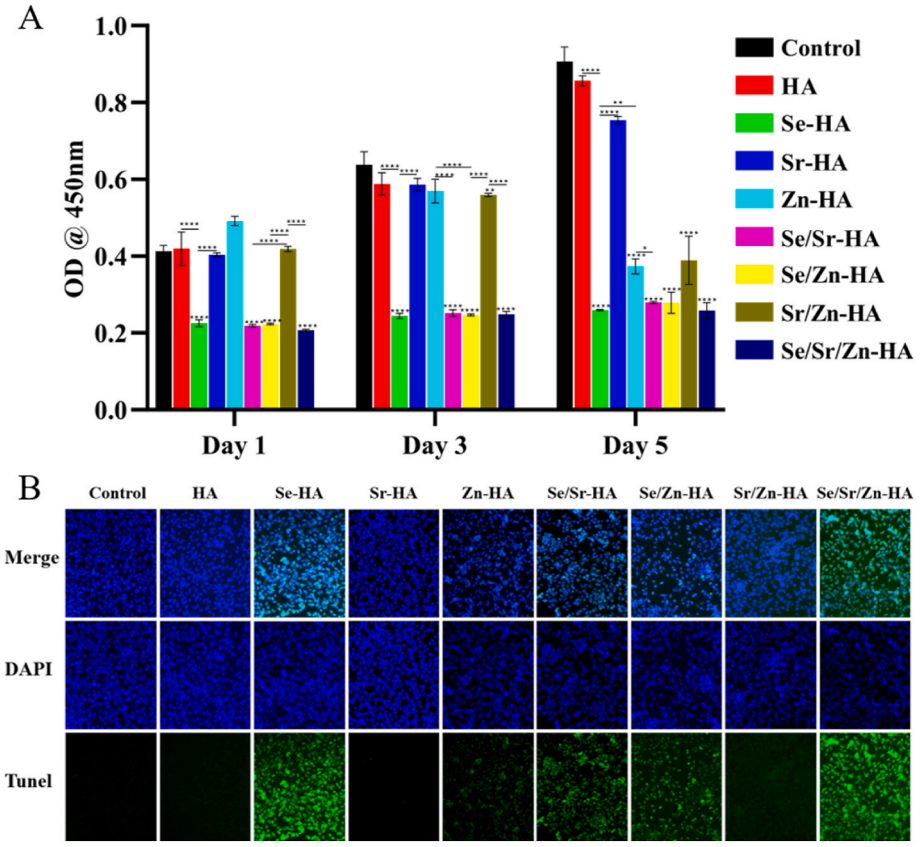

Fig. 7. Anti-tumor evaluation of 143b by culturing with HA, Se-HA, Sr-HA, Zn-HA, Se/Sr-HA, Se/Zn-HA, Sr/Zn-HA, and Se/Sr/Zn-HA extracts *in vitro*. (A) The OD value of 143b on 1 d, 3 d, and 5 d. (B) Tunel staining of 143b on day 3. (n = 3, *p < 0.05, **p < 0.01, ***p < 0.001, ****p < 0.0001.)

the amount of 143b in the material group was lower than that in the control group. In addition, the amount of 143b in Zn-HA was higher than those in Sr-HA and the control after 1 day of culture, while after 5 days of co-culture, the amount of 143b in Zn-HA was lower than that in Sr-HA, indicating that the time required for Zn^{2+} to exert its anti-tumor effect was longer. Zn^{2+} released from Zn-based biomaterials can significantly inhibit the proliferation of various tumors via an apoptosis-inducing effect [84]. After 5 days of culture, the anti-tumor effect of the double-element doping HA, except the Sr/Zn-HA, was superior to those of the single-element doping and control groups, which were related to the weaker anti-tumor effects of Sr^{2+}. Although Sr^{2+} showed weak anti-tumor ability, the anti-tumor efficiency of Sr-HA was still higher than that of HA and control groups. Karim et al. had demonstrated that Sr^{2+} possessed anti-tumor properties [85]. However, the amount of 143b in Se/Sr/Zn-HA was significantly lower than that in the control and non-SeO_3^{2-} groups throughout the co-culture period, indicating an excellent and long-lasting anti-tumor effect of Se/Sr/Zn-HA. SeO_3^{2-} and Zn^{2+} combined administration or SeO_3^{2-} and Sr^{2+} combined administration displayed better antitumor effects [69,86]. Tunel staining results showed that the survival rate of 143b was the lowest after 3 days of culture with Se-HA and Se/Sr/Zn-HA, as shown in Fig. 7B. Furthermore, SeO_3^{2-} containing extracts showed an excellent anti-tumor effect, while almost no 143b apoptosis was observed in the control group, HA, and Sr-HA, which was consistent with the results of quantitative statistics. To further confirm the synergistic anti-tumor effect of SeO_3^{2-}, Sr^{2+}, and Zn^{2+}, the extracts of HA, Se-HA, Sr-HA, Zn-HA, and Se/Sr/Zn-HA were used to culture with MG-63 and UMR-106. Fig. S3A showed the amount of MG-63 in experimental groups decreased relative to those of the control group after one day of incubation, while the amounts of MG-63 in Se-HA and Se/Sr/Zn-HA were the least. However, the amounts of MG-63 in Se-HA and Se/Sr/Zn-HA continued to decrease, and the quantity of MG-63 in other groups increased variably after 3 days of incubation. Flow cytometry showed that MG-63 had the lowest survival rate in Se/Sr/Zn-HA and was the most apoptotic during the late stage, as shown in Fig. S3B, which was similar to 143b. The above data indicated that SeO_3^{2-} displayed the most significant inhibitory effect on MG-63, while the inhibitory effect on MG-63 of Se/Sr/Zn-HA was higher than Se-HA, which may be attributed to the higher doping efficiency of SeO_3^{2-} in Se/Sr/Zn-HA (Table 1) and higher content of SeO_3^{2-} released from Se/Sr/Zn-HA during the same time (Fig. 3D). Wei. et al. synthesized Sr-SeHA (Sr-SeHA) and reported that Sr^{2+} was non-toxic to MG-63, but SeO_3^{2-} can inhibit the proliferation of MG-63 [69]. The results of fluorescence staining of living and dead cells demonstrated that the survival rate of UMR-106 was the lowest after 3 days by culturing with Se-HA and Se/Sr/Zn-HA, as shown in Fig. S3C. The results of fluorescence staining further confirmed the inhibitory effect of SeO_3^{2-} on UMR-106, and the dead cells of Se/Sr/Zn-HA were slightly more than those of Se-HA, indicating that the death of UMR-106 was dependent on the concentration of SeO_3^{2-}. Generally, Se-HA and Se/Sr/Zn-HA showed the best anti-tumor effects, and the incorporation of Sr^{2+} and Zn^{2+} did not significantly weaken the anti-tumor effect of SeO_3^{2-}.

3.6. Characterization of HA-PCLs, Se-HA-PCLs, Sr-HA-PCLs, Zn-HA-PCLs, and Se/Sr/Zn-HA-PCLs

The surface morphology and cross-sectional element distribution of the composite scaffold were observed with a scanning electron microscope equipped with an EDS spectrometer. Since the viscosity and plasticity of the PCL, its processing can be facilitated by the narrow nozzle extrusion adopted in 3D printing technology, providing the required rheological properties for the structural stability of the bracket and layer during printing [87]. In addition, HA-PCLs could evade the inherent brittleness of pure HA scaffolds, and the resultant scaffolds could degrade slowly, and retain their morphology and mechanical properties after implantation with the compatible degradation timescale as the time required for tissue regeneration [88]. Therefore, PCL was introduced with HA to construct porous scaffolds in this study. After mixing PCL with HA, the PCL film was filled with a large amount of HA powder so that the degradation speed of the composite scaffold was accelerated compared with pure PCL scaffold. Meanwhile, the HA powder inside the composite scaffold was exposed and exerted biological function [89]. The surface morphology of several scaffolds: HA-PCLs, Se-HA-PCLs, Sr-HA-PCLs, Zn-HA-PCLs, and Se/Sr/Zn-HA-PCLs were shown in Fig. 8A. All the composite scaffolds exhibited uniform and mutually penetrating 3D porous structures with a macropore size of approximately 350 μm. Referring to cell size, migration requirements, and transport, the minimum pore size required was approximately 100 μm, and a pore size greater than 300 μm was recommended due to enhanced new bone formation and capillary formation [90]. Therefore, the macropore size of the composite scaffold was conducive to the ingrowth of blood vessels and the regeneration of new bone. The surface morphologies of Sr-HA-PCLs and Se/Sr/Zn-HA-PCLs were rough, while the other groups showed smooth surface morphologies, which may be related to the morphologies of Sr-HA and Se/Sr/Zn-HA. Related studies have shown that a degree of roughness of the material surface was conducive to cell adhesion and spreading and enhances the osteogenic properties of materials [91]. The cross-sectional element distribution of Se/Sr/Zn-HA-PCLs was shown in Fig. 8B, and the cross-section revealed a regular circular profile with a diameter of approximately 400 μm. Se, Sr, and Zn were uniformly distributed within the scaffold, indicating that the element-doped HA and PCL were uniformly mixed. To confirm that dichloromethane had been removed, the chemical structures of composite scaffolds were examined by FTIR, as shown in Fig. S8. There was no characteristic functional group of di-chloromethane comprised in the composite scaffold, indicating that di-chloromethane has been completely removed, which was consistent with the results of previous studies [92]. The fidelity of the composite scaffolds was higher than 70%, indicating that the composite scaffolds fabricated by 3D printing technology matched the designed scaffold well, as shown in Fig. S9. The HA-PCLs and Sr-HA-PCLs possessed higher fidelity, which was attributed to the higher density of HA and Sr-HA. Due to the low density of Se-HA and Zn-HA, the fidelity of Se-HA-PCLs and Zn-HA-PCLs was lower, while the fidelity of Se/Sr/Zn-HA-PCLs was intermediate. The mechanical property of the scaffold as a bone substitute lies in its compressive strength, which requires resistance to wear caused by movement or pressure of the surrounding tissue [93]. The compressive modulus and stress-strain curve of the composite scaffolds were shown in Fig. S10. There was no significant difference in the compressive modulus of the composite scaffolds, all of which were over 25 MPa. The compressive modulus of cancellous bone was 2–13 MPa, and the mechanical properties of the composite scaffolds fabricated in the current study met the needs of bone repair scaffolds [94]. To verify the anti-tumor potential of composite scaffolds, Se-HA-PCLs, Sr-HA-PCLs, Zn-HA-PCLs, and Se/Sr/Zn-HA-PCLs were soaked in acidic PBS and the release of SeO_3^{2-}, Sr^{2+}, and Zn^{2+} was detected, as shown in Table S4. Although the release of Sr^{2+} and Zn^{2+} in Se/Sr/Zn-HA-PCLs was lower than that of Sr^{2+} and Zn^{2+} in Sr-HA-PCLs and Zn-HA-PCLs, respectively, the release of SeO_3^{2-} was higher than that of Se-HA-PCLs, indicating that the anti-tumor potentials of Se/Sr/Zn-HA-PCLs was superior to Se-HA-PCLs *in vivo*. Hiraoka et al. had confirmed that when the concentration of SeO_3^{2-} reached 20 μg/L, it can effectively inhibit the proliferation of osteosarcoma cells [95]. The concentration of SeO_3^{2-} of Se/Sr/Zn-HA-PCLs was 188.56 μg/L, which could effectively inhibit the proliferation of osteosarcoma cells, endowing Se/Sr/Zn-HA-PCLs a great anti-tumor potential.

3.7. Evaluation of the anti-tumor potentials of HA and element-doped HA in vivo

The powder of HA, Se-HA, Sr-HA, Zn-HA, Se/Sr-HA, Se/Zn-HA, Sr/Zn-HA, and Se/Sr/Zn-HA was respectively mixed with PBS and injected into the tumor of tumor-bearing mice. The anti-tumor potentials were

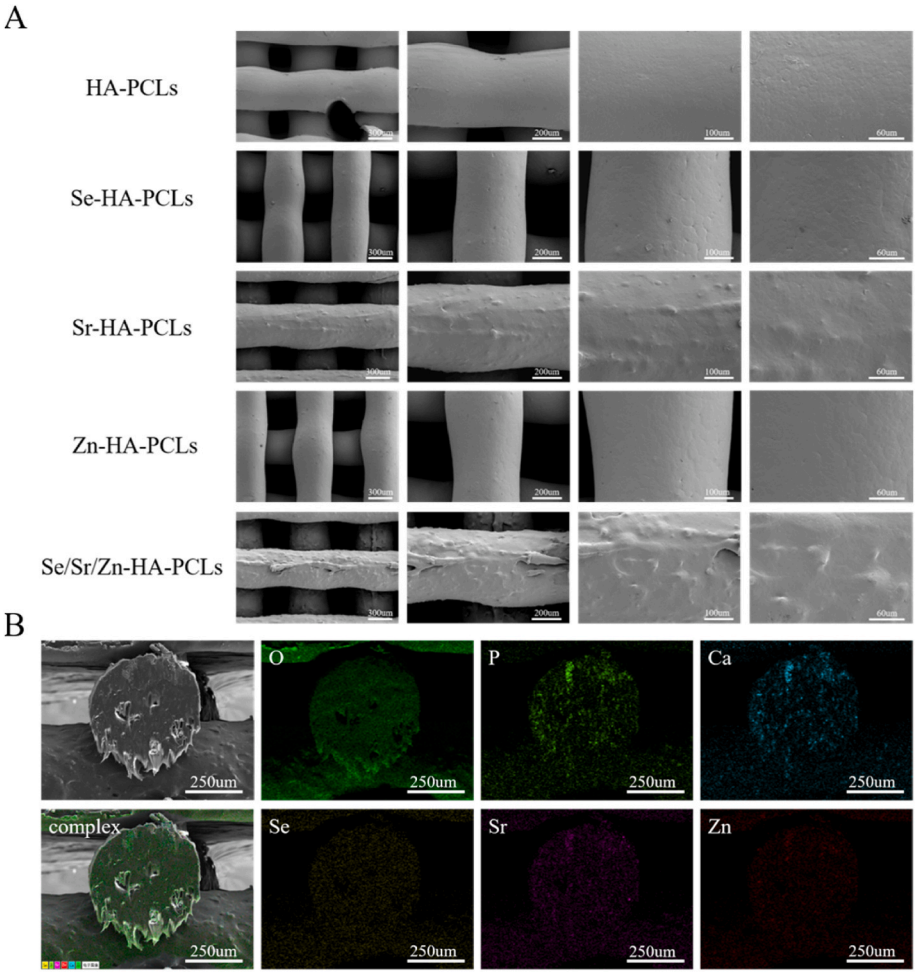

Fig. 8. Characterization of HA-PCLs, Se-HA-PCLs, Sr-HA-PCLs, Zn-HA-PCLs, and Se/Sr/Zn-HA-PCLs. (A) SEM images. (B) Element mapping of the cross-section of Se/Sr/Zn-HA-PCLs.

evaluated by determining the size of the subcutaneous tumor in the mice. The subcutaneous tumors were extracted and photographed after sacrificing the mice, as shown in Fig. 9A. The tumors in the PBS-injected mice increased significantly, while those of the HA-treated mice were not significantly inhibited although they were slightly smaller than those of PBS-treated. The inhibition of the tumor by HA was attributed to the dissolution of HA in the acidic environment of the tumor and the release of a large number of Ca^{2+}, resulting in the overload of Ca^{2+} and the apoptosis of tumor cells [17,96]. The anti-tumor effects of Sr-HA, Zn-HA, and Sr/Zn-HA were similar to those of HA, suggesting that Sr^{2+} and Zn^{2+} contained poor antitumor effects, which were in line with the anti-tumor results *in vitro*. Although the antitumor effect of Zn-HA was indisposed, Gao et al. had confirmed that Zn^{2+} can inhibit the proliferation and invasion of osteosarcoma cells and promote the apoptosis of osteosarcoma cells by activating the Wnt-3a/β-catenin signaling pathway [97]. The tumor sizes of Se-HA, Se/Sr-HA, Se/Zn-HA, and Se/Sr/Zn-HA were smaller than other groups significantly, indicating that SeO_3^{2-} had a better anti-tumor effect than Sr^{2+}, and Zn^{2+}. The anti-tumor effects of Se/Sr-HA and Se/Zn-HA were comparable to those of Se-HA, indicating that the incorporation of Sr^{2+} and Zn^{2+} did not impair the anti-tumor effects of SeO_3^{2-}, which was consistent with the anti-tumor results *in vitro*. However, the mice treated with Se/Sr/Zn-HA had the smallest tumors (Fig. 9B), indicating that the synergistic administration of SeO_3^{2-}, Sr^{2+}, and Zn^{2+} resulted in the best anti-tumor effect *in vivo* (n = 3). The synergistic doping of SeO_3^{2-}, Sr^{2+}, and Zn^{2+} not only reduced the crystallinity of HA, but also improved the doping efficiency and release efficiency of SeO_3^{2-}, Sr^{2+}, or Zn^{2+}, thus further improving the anti-tumor effect [62]. Tumor cell apoptosis was analyzed by hematoxylin and eosin (H&E) (Fig. 9C) and Ki67 staining (Fig. 9D) after tumor fixation. The results revealed that the tumor cell of the control group did not undergo obvious apoptosis, and HA, Sr-HA, Zn-HA, and Sr/Zn-HA displayed similar effects, showing subtle anti-tumor effects. The quantified live tumor cell area of Ki67 staining showed similar results, as shown in Fig. S6. Bone-mimetic Se-HA could induce more tumor cell apoptosis in tumor tissues substantiated by H&E and Ki67 staining [32]. However, tumors treated with Se-HA, Se/Sr-HA, Se/Zn-HA, and Se/Sr/Zn-HA showed significant tumor cell apoptosis, and their anti-tumor effects were better than those of the control group, HA, Sr-HA, Zn-HA, and Sr/Zn-HA, which was consistent with the *in vitro* results. Wang et al. found that Se-HA induced apoptosis of tumor cells through an intrinsic caspase-dependent apoptotic pathway coordinated by the production of reactive oxygen species [31]. Terminal deoxynucleotidyl transferase-mediated nickel-end labeling of dUTP (TUNEL) staining also exhibited similar results, namely SeO_3^{2-}-containing experimental group induced more tumor cells apoptosis, especially Se/Sr/Zn-HA, as shown in Fig. S4. In addition, the tumor inhibition rate of the experimental group was significantly different from that of the control group on day 8 after sample treatment, the SeO_3^{2-}-containing experimental group got better tumor inhibitory effects, and the tumor inhibition rate of Se/Sr/Zn-HA was highest, as shown in Fig. S5. *In vivo* antitumor results demonstrated that SeO_3^{2-} displayed excellent anti-tumor effects, and the synergistic administration of SeO_3^{2-}, Sr^{2+}, and Zn^{2+} possessed the best antitumor effects.

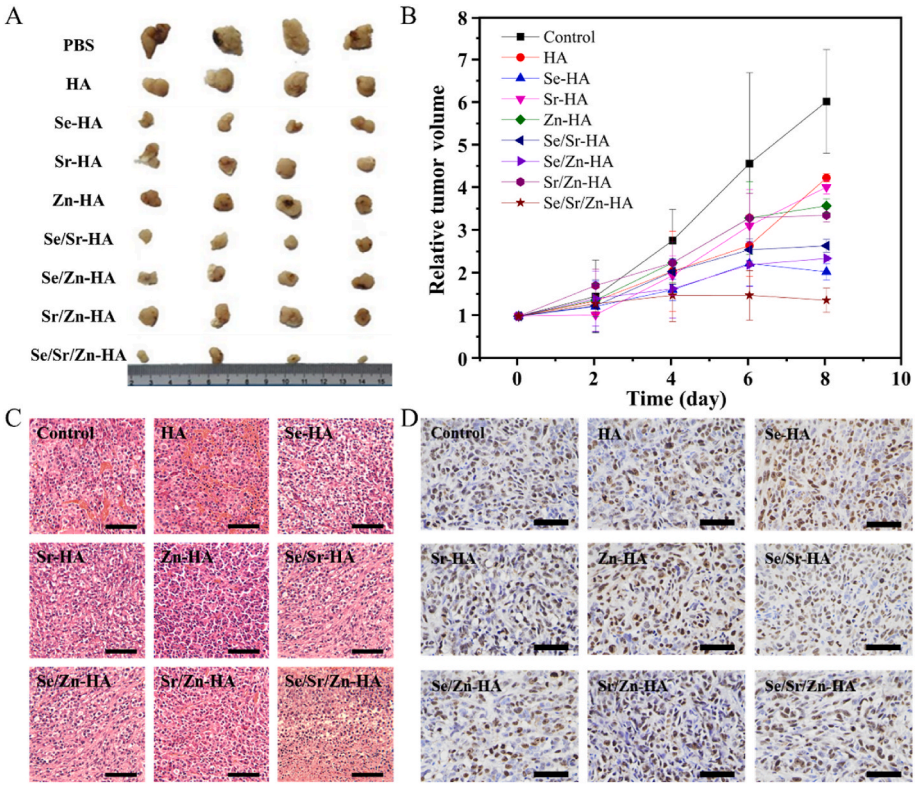

Fig. 9. Evaluation of the anti-tumor properties of HA, Se-HA, Sr-HA, Zn-HA, Se/Sr-HA, Se/Zn-HA, Sr/Zn-HA, and Se/Sr/Zn-HA. (A) Tumors were extracted after the mice were sacrificed. (B) Relative tumor volume changes over time after sample injection. (C) H&E staining of tumor tissue on day 8, scale bar: 100 μm. (D) Ki67 staining for tumor tissue on day 8, scale bar: 100 μm. (n = 3).

3.8. Biosafety evaluation of HA and element-doped HA in vivo

To evaluate the biological safety of the materials injected into the body, sections of major organs of mice, including the heart, liver, spleen, lung, and kidney were stained with H&E, as shown in Fig. 10. The heart, liver, spleen, lung, and kidney showed no obvious histological lesion can be observed, which was in line with the previous study [31]. In addition, the changes in the weights of the mice over time after the sample injection for 8 days was similar: the changes were the extension of feeding time and a slow increase in weight, as shown in Fig. S7. These results demonstrated that HA, Se-HA, Sr-HA, Zn-HA, Se/Sr-HA, Se/Zn-HA, Sr/Zn-HA, and Se/Sr/Zn-HA caused no damage to the heart, liver, spleen, lung, and kidney of the mice, confirming the biological safety of all injected materials for anti-tumor treatment *in vivo*.

3.9. The osteogenic differentiation potentials of HA-PCLs, Se-HA-PCLs, Sr-HA-PCLs, Zn-HA-PCLs, and Se/Sr/Zn-HA-PCLs in vivo

The osteogenic properties of HA-PCLs, Se-HA-PCLs, Sr-HA-PCLs, Zn-HA-PCLs, and Se/Sr/Zn-HA-PCLs were evaluated by repairing femoral defects in rats. H&E and Masson staining were used to evaluate the bone repair effect, as shown in Fig. 11. H&E staining showed that the osteogenic effect of HA-PCLs, Se-HA-PCLs, Sr-HA-PCLs, Zn-HA-PCLs, and Se/Sr/Zn-HA-PCLs was better than that of the control group, and the osteogenic effect of Se-HA-PCLs, Sr-HA-PCLs, and Zn-HA-PCLs was superior to that of HA-PCLs. Relevant studies have demonstrated that the osteogenesis performance of Se-HA was better than those of HA [33,75]. The osteogenic effect of Sr-HA-PCLs and Zn-HA-PCLs were similar, furthermore, Sr-HA-PCLs was similar to that of the control group. Zakhireh et al. fabricated a Se-doped HA scaffold that showed excellent anti-tumor activity and significantly improved the expression of osteogenic-related proteins compared to HA [75]. Similarly, Wei et al. synthesized a Se/Sr double-doped HA that showed good biocompatibility with and Zn-HA-PCLs were slightly better than Se-HA-PCLs, while Se/Sr/Zn-HA-PCLs showed the best osteogenic effect. Compared with Se-HA, Sr-HA contained a better effect on promoting the proliferation of osteoblast-like human cells [62]. Wang et al. fabricated a Zn/Sr co-doped HA porous scaffold that showed better osteoinductivity and antibacterial properties than Zn or Sr-doped HA porous scaffolds [63]. Masson staining displayed similar results as H&E staining: HA-PCLs was better than the control group, while Se-HA-PCLs, Sr-HA-PCLs, and Zn-HA-PCLs were better than HA-PCLs, and Se/Sr/Zn-HA-PCLs possessed the best repair effect. The above results confirmed that SeO_3^{2-}, Sr^{2+}, or Zn^{2+} can improve the osteogenic property of HA, and the effect of three elements doped HA was greater than that of a single element doped HA, which was similar to the ALP activity of the extract co-culture with MSCs *in vitro* (except that the ALP activity of Zn-HA treated mBMSCs) and inhibited the activity of MG-63 effectively [69]. In this study, SeO_3^{2-}, Sr^{2+}, and Zn^{2+} collaboratively improved the bioactivity of HA, which exhibited better bone-promoting, anti-tumor, and antibacterial effects than HA or single-element doped HA, thus significantly improving the efficiency of bone-repairing and reducing the risk of tumor recurrence.

In the current study, Se/Sr/Zn-HA-PCLs was fabricated to repair bone defects and prevent tumor recurrence after resection of osteosarcoma. SeO_3^{2-}, Sr^{2+}, and Zn^{2+} were gradually released from Se/Sr/Zn-HA and exposed to the tissue environment after the degradation of PCL. SeO_3^{2-} possessed an excellent anti-tumor effect and displayed a good osteogenic effect. However, a large number of studies only focused on the anti-tumor function of SeO_3^{2-}, but paid little attention to osteogenesis ability [98,99]. The expression level of ALP in Se-HA and Se/Sr/Zn-HA was higher than that of the HA group after administration for 14 days, and there was a significant difference compared with the control group (Fig. 6A). Compared with HA, Se-HA could significantly up-regulate the expression of ALP after administration for 7 and 14 days. In addition, related studies had confirmed that Se-HA could promote the

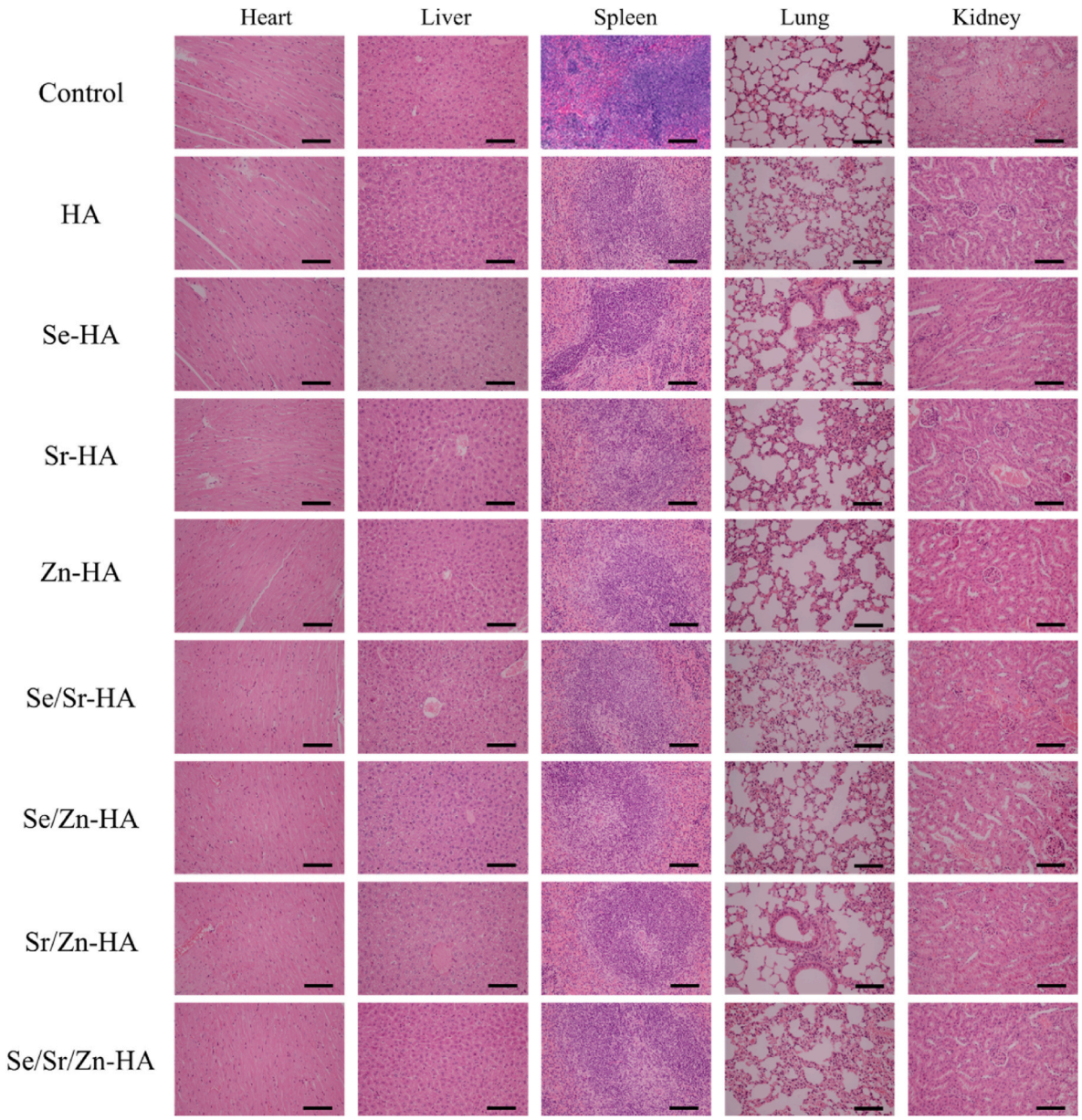

Fig. 10. H&E staining of the heart, liver, spleen, lung, and kidney on day 8; scale bar: 100 μm.

expression of osteogenesis-related genes, such as osteocalcin and type I collagen [100]. These results suggested that free SeO_3^{2-} released from Se-HA could promote osteogenic differentiation of MSCs. As an effective antioxidant and free radical scavenger, SeO_3^{2-} could reduce the ROS of MSCs, which may be in favor of the osteogenic differentiation of MSCs [101,102]. About 98% of strontium in the human body is located in bone tissue, and the osteogenic effect of Sr^{2+} has been confirmed by a large number of studies [103]. In recent years, strontium ranelate had become a drug for the treatment of osteoporosis [104]. Sr^{2+} enhanced the expression of osteogenic marker genes such as *Runx2*, *OCN*, osteopontin (*OPN*), bone salivary protein (*BSP*), and type I collagen, increased ALP activity and matrix mineralization, promoted osteogenic differentiation of MSCs [29]. The expression of ALP in Sr-HA and Se/Sr/Zn-HA was significantly higher than that of HA and control groups, indicating that Sr^{2+} could promote the expression of ALP in MSC. In addition, other studies had shown that Sr^{2+} can up-regulate the expression of endogenous *BMP-2* [20]. Se/Sr-HA displayed good biocompatibility and could promote the proliferation of MSC, which may be beneficial to the osteogenic differentiation of MSC [105]. Zinc is a necessary trace element for many cellular catalysis, structure, and regulation processes [106]. Zinc can promote bone formation by inducing collagen synthesis, enhancing ALP activity, and bone nodule mineralization. Although there was no significant difference in ALP activity between Zn-HA and the control group in this study, the expression of ALP in 14 days was higher than that in 7 days, which was related to a high concentration of Zn^{2+} [78]. In addition, Zn^{2+} decreased bone resorption by antagonizing NF-κB activation and inhibiting osteoclast differentiation [107]. Wang et al. had confirmed that the ALP activity of Sr/Zn-HA was higher than that of Sr-HA and Zn-HA, indicating that the synergistic administration of Sr^{2+} and Zn^{2+} revealed a stronger effect on promoting osteogenic differentiation of MSCs [63]. SeO_3^{2-}, Sr^{2+}, and Zn^{2+} can promote the expression of ALP in MSCs, therefore, the ALP activity of Se/Sr/Zn-HA was higher than that of Se-HA, Sr-HA, and Zn-HA.

The results of femoral defect repair *in vivo* were consistent with those of osteogenic differentiation *in vitro*, namely the repair effect of Se-HA-PCLs, Sr-HA-PCLs, and Zn-HA-PCLs was better than that of HA-PCLs and control group, and Se/Sr/Zn-HA-PCLs had the best repair effect, as shown in Fig. 11. Collectively, SeO_3^{2-}, Sr^{2+}, Zn^{2+}, and Ca^{2+} released

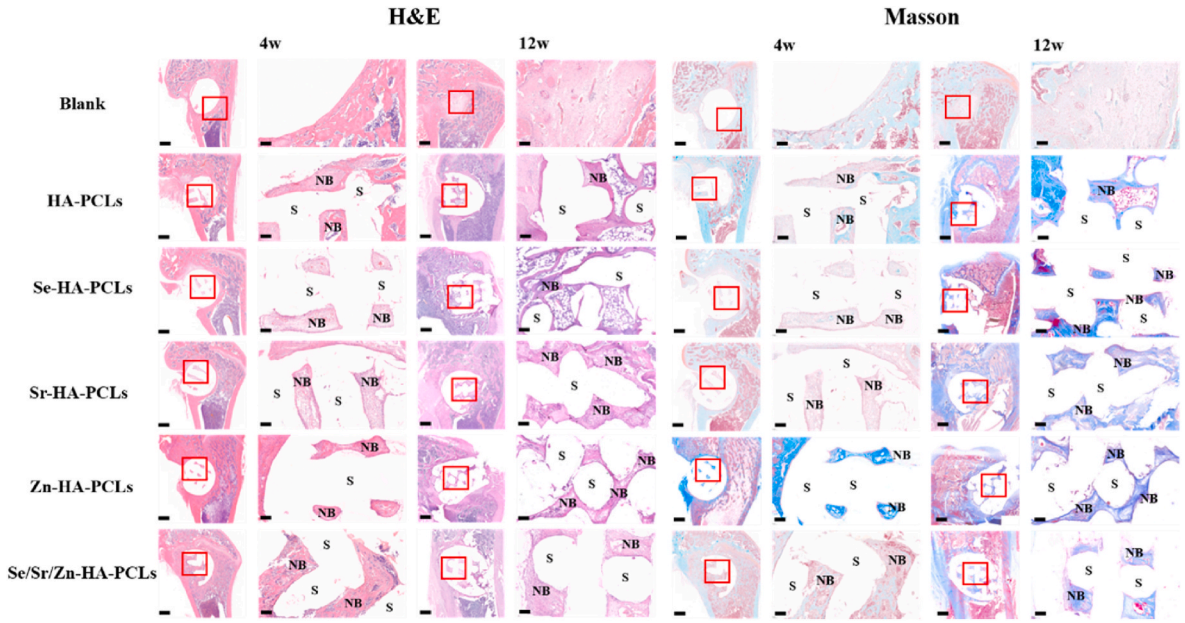

Fig. 11. H&E and Masson staining of bone formation after composite scaffold implantation for 4 and 12 weeks; S represents scaffold, NB represents new bone; scale bar:1000 μm, enlarged area scale bar: 100 μm.

from Se/Sr/Zn-HA-PCLs could effectively induce osteogenic differentiation of MSCs and ultimately repair femoral defects.

4. Conclusions

In this study, HA, single element doped, double elements doped, and three elements doped HA were successfully synthesized using the hydrothermal method. *In vitro* study confirmed that the extracts of HA, Se-HA, Sr-HA, Zn-HA, Se/Sr-HA, Se/Zn-HA, Sr/Zn-HA, and Se/Sr/Zn-HA displayed good biocompatibility, SeO_3^{2-} possessed excellent anti-tumor activities, SeO_3^{2-}, Sr^{2+}, and Zn^{2+} showed better potential for promoting osteogenic differentiation, while Zn^{2+} also revealed good antibacterial properties. However, the synergistic administration of SeO_3^{2-}, Sr^{2+}, and Zn^{2+} could achieve better anti-tumor, osteogenesis, and antibacterial effects. Consequently, Se/Sr/Zn-HA presented excellent anti-tumor, osteogenesis, and antibacterial potential *in vitro*. The *in vivo* anti-tumor evaluation demonstrated that Se-HA, Se/Sr-HA, Se/Zn-HA, and Se/Sr/Zn-HA exhibited better anti-tumor effects compared to those of HA, Sr-HA, Zn-HA, and Sr/Zn-HA, while Se/Sr/Zn-HA revealed the most obvious anti-tumor effect without causing toxic side effects to normal organs. Furthermore, HA-PCLs, Se-HA-PCLs, Sr-HA-PCLs, Zn-HA-PCLs, and Se/Sr/Zn-HA-PCLs fabricated by 3D printed displayed admirable femoral repair effects *in vivo*, and the osteogenic effects of Se/Sr/Zn-HA-PCLs were the best. The Se/Sr/Zn-HA-PCLs with excellent anti-tumor, osteogenic effects, and antibacterial potential could be a potential candidate to be employed in repairing bone defects after the resection of bone tumors.

Ethics approval and consent to participate

The animal surgical procedures involved in this study follow the recommendations of the Animal Care and Experiment Committee of Shanghai Ninth People's Hospital, Shanghai Jiao Tong University School of Medicine (SH9H-2021-A433-SB).

Credit Author Statement

Hao Huang: Conceptualization, Methodology, Writing – original draft. Lei Qiang: Methodology, Formal analysis, Writing – review & editing. Minjie Fan: Validation, Writing – review & editing. Yihao Liu: Writing – review & editing. Anchun Yang: Material synthesis and characterization. Dongbiao Chang: Data analysis. Jinsheng Li: Graphics modification and layout. Tong Sun: Idea of experiment. Yiwei Wang: In vitro experiment design. Ruoyi Guo: In vitro experimental model construction. Hanjie Zhuang: Participating in in vivo experiments. Xiangyu Li: Printing scaffolds. Tailin Guo: Revision of manuscript. Jinwu Wang: Writing – review & editing. Huan Tan: Supervision on in vitro cell experiments. Pengfei Zheng: Supervision, Project administration, Funding acquisition. Jie Weng: Supervision, Funding acquisition.

Declaration of competing interest

The authors declare that they have no known competing financial interests or personal relationships that could have appeared to influence the work reported in this paper.

Acknowledgments

This work was supported by the National Natural Science Foundation of China (52071277, 21802009); Jiangsu Provincial Key Research and Development Program (CN) (BE2019608); China Postdoctoral Science Foundation (2022M721685); Jiangsu Health Commission Medical Research Program (2020158); National Facility for Translational Medicine (Shanghai) Open Program (TMSK-2021-304); 2020 Nanjing International Science and Technology Cooperation Program; Nanjing Medical Science and Technology Development Key Program (ZKX18041).

Appendix A. Supplementary data

Supplementary data to this article can be found online at https://doi.org/10.1016/j.bioactmat.2023.07.004.

References

[1] C. Li, W. Zhang, R. Wang, X. Liang, L. Qin, Y. Lai, Nanocomposite multifunctional hydrogel for suppressing osteosarcoma recurrence and enhancing bone regeneration, Chem. Eng. J. 435 (2022), 134896, https://doi.org/10.1016/j.cej.2022.134896.
[2] J. Ritter, S. Bielack, Osteosarcoma, Ann. Oncol. 21 (2010) 320–325, https://doi.org/10.1093/annonc/mdq276.

[3] J. Liao, R. Han, Y. Wu, Z. Qian, Review of a new bone tumor therapy strategy based on bifunctional biomaterials, Bone. Res 9 (1) (2021) 18, https://doi.org/10.1038/s41413-021-00139-z.

[4] D. Zhang, S. Cheng, J. Tan, J. Xie, Y. Zhang, S. Chen, H. Du, S. Qian, Y. Qiao, F. Peng, X. Liu, Black Mn-containing layered double hydroxide coated magnesium alloy for osteosarcoma therapy, bacteria killing, and bone regeneration, Bioact. Mater. 17 (2022) 394–405, https://doi.org/10.1016/j.bioactmat.2022.01.032.

[5] A. Luetke, P.A. Meyers, I. Lewis, H. Juergens, Osteosarcoma treatment – where do we stand? A state of the art review, Cancer Treat Rev. 40 (4) (2014) 523–532, https://doi.org/10.1016/j.ctrv.2013.11.006.

[6] M.S. Isakoff, S.S. Bielack, P. Meltzer, R. Gorlick, Osteosarcoma: current treatment and a collaborative pathway to success, J. Clin. Oncol. 33 (27) (2015) 3029–3035, https://doi.org/10.1200/jco.2014.59.4895.

[7] Y.H. Han, C.G. Liu, B.Q. Chen, C.P. Fu, R.K. Kankala, S.B. Wang, A.Z. Chen, Orchestrated tumor apoptosis (Cu^{2+}) and bone tissue calcification (Ca^{2+}) by hierarchical Copper/Calcium-ensembled bioactive silica for osteosarcoma therapy, Chem. Eng. J. 435 (2022), 134820, https://doi.org/10.1016/j.cej.2022.134820.

[8] S.E. Leary, A. Wozniaks, C.A. Billups, J. Wu, V. Mcpherson, M. Neel, B.N. Rao, N. C. Daw, Survival of pediatric patients after relapsed osteosarcoma: the St. Jude Children's Research Hospital experience, J. Clin. Oncol. 119 (14) (2013) 2645–2653, https://doi.org/10.1200/jco.2008.26.15_suppl.10516.

[9] R. Lin, C. Deng, X. Li, Y. Liu, C.T. Wu, Copper-incorporated bioactive glass-ceramics inducing anti-inflammatory phenotype and regeneration of cartilage/bone interface, Theranostics 9 (21) (2019) 6300–6313, https://doi.org/10.7150/thno.36120.

[10] J.C. Moses, S.K. Nandi, B.B. Mandal, Multifunctional cell instructive silk-bioactive glass composite reinforced scaffolds toward osteoinductive, proangiogenic, and resorbable bone grafts, Adv. Healthc. Mater. 7 (10) (2018), e1701418, https://doi.org/10.1002/adhm.201701418.

[11] F. Foroughi, A. Bigham, E.R. Ghomi, M. Rafienia, H. Luo, F. Khosravi, S. Ramakrishna, Multifunctional bone scaffolds: from regeneration to bone cancer therapy, Biomed. J. Sci. Tech. Res. 27 (5) (2020), https://doi.org/10.26717/BJSTR.2020.27.004572, 2574 -1241.

[12] H. Yang, H. Gao, Y. Wang, Hollow hydroxyapatite microsphere: a promising carrier for bone tissue engineering, J. Microencapsul. 33 (5) (2016) 421–426, https://doi.org/10.1080/02652048.2016.1202347.

[13] H. Zhang, H. Huang, G. Hao, Y. Zhang, H. Ding, Z. Fan, L. Sun, 3D printing hydrogel scaffolds with nanohydroxyapatite gradient to effectively repair osteochondral defects in rats, Adv. Funct. Mater. 31 (1) (2020), 2006697, https://doi.org/10.1002/adfm.202006697.

[14] H. Huang, A. Yang, J. Li, T. Sun, S. Yu, X. Lu, T. Guo, K. Duan, P. Zheng, J. Weng, Preparation of multigradient hydroxyapatite scaffolds and evaluation of their osteoinduction properties, Regen. Biomater. 9 (2022), https://doi.org/10.1093/rb/rbac001 rbac001.

[15] M.C. Lee, H. Seonwoo, K.J. Jang, S. Pandey, J. Lim, S. Park, J.E. Kim, Y. H. Choung, P. Garg, J.H. Chung, Development of novel gene carrier using modified nano hydroxyapatite derived from equine bone for osteogenic differentiation of dental pulp stem cells, Bioact. Mater. 6 (9) (2021) 2742–2751, https://doi.org/10.1016/j.bioactmat.2021.01.020.

[16] Y. Hu, S. Cao, J. Chen, Y. Zhao, F. He, Q. Li, L. Zou, C. Shi, Biomimetic fabrication of icariin loaded nano hydroxyapatite reinforced bioactive porous scaffolds for bone regeneration, Chem. Eng. J. 394 (2020), 124895, https://doi.org/10.1016/j.cej.2020.124895.

[17] K. Zhang, Y. Zhou, C. Xiao, W. Zhao, H. Wu, X. Zhu, C. Tu, X. Zhang, Application of hydroxyapatite nanoparticles in tumor-associated bone segmental defect, Sci. Adv. 5 (2019), eaax6946, https://doi.org/10.1126/sciadv.aax6946.

[18] F. Liu, B. Sun, X. Jiang, S. Aldeyab, Q. Zhang, M. Zhu, Mechanical properties of dental resin/composite containing urchin-like hydroxyapatite, Dent. Mater. 30 (12) (2014) 1358–1368, https://doi.org/10.1016/j.dental.2014.10.003.

[19] H. Zhang, B.W. Darvell, Mechanical properties of hydroxyapatite whisker-reinforced bis-GMA-based resin composites, Dent. Mater. 28 (8) (2012) 824–830, https://doi.org/10.1016/j.dental.2012.04.030.

[20] E. O'Neill, G. Awale, L. Daneshmandi, O. Umerah, K.W. Lo, The roles of ions on bone regeneration, Drug Discov. Today 23 (4) (2018) 879–890, https://doi.org/10.1016/j.drudis.2018.01.049.

[21] M. Dermience, G. Lognay, F. Mathieu, P. Goyens, Effects of thirty elements on bone metabolism, J. Trace Elem. Med. Biol. 32 (2015) 86–106, https://doi.org/10.1016/j.jtemb.2015.06.005.

[22] S. Bose, G. Fielding, S. Tarafder, A. Bandyopadhyay, Understanding of dopant-induced osteogenesis and angiogenesis in calcium phosphate ceramics, Trends, Biotechnol. 31 (10) (2013) 594–605, https://doi.org/10.1016/j.tibtech.2013.06.005.

[23] M. Hu, J. Fang, Y. Zhang, X. Wang, W. Zhong, Z. Zhou, Design and evaluation a kind of functional biomaterial for bone tissue engineering: selenium/mesoporous bioactive glass nanospheres, J. Colloid Interface Sci. 579 (2020) 654–666, https://doi.org/10.1016/j.jcis.2020.06.122.

[24] C.M. Beukhof, M. Medici, A.W. van den Beld, B. Hollenbach, A. Hoeg, W.E. Visser, W.W. de Herder, T.J. Visser, L. Schomburg, R.P. Peeters, Selenium status is positively associated with bone mineral density in healthy aging European men, PLoS One 11 (4) (2016), e0152748, https://doi.org/10.1371/journal.pone.0152748.

[25] J. Qiu, L. Liu, B. Chen, Y. Qiao, H. Cao, H. Zhu, X. Liu, Graphene oxide as a dual Zn/Mg ion carrier and release platform: enhanced osteogenic activity and antibacterial properties, J. Mater. Chem. B 6 (13) (2018) 2004–2012, https://doi.org/10.1039/c8tb00162f.

[26] G. Jin, H. Qin, H. Cao, S. Qian, Y. Zhao, X. Peng, X. Zhang, X. Liu, P.K. Chu, Synergistic effects of dual Zn/Ag ion implantation in osteogenic activity and antibacterial ability of titanium, Biomaterials 35 (27) (2014) 7699–7713, https://doi.org/10.1016/j.biomaterials.2014.05.074.

[27] R. Zhao, S. Chen, W. Zhao, L. Yang, B. Yuan, V.S. Ioan, A.V. Iulian, X. Yang, X. Zhu, X. Zhang, A bioceramic scaffold composed of strontium-doped three-dimensional hydroxyapatite whiskers for enhanced bone regeneration in osteoporotic defects, Theranostics 10 (4) (2020) 1572–1589, https://doi.org/10.7150/thno.40103.

[28] N. Baheiraei, H. Eyni, B. Bakhshi, R. Najafloo, N. Rabiee, Effects of strontium ions with potential antibacterial activity on in vivo bone regeneration, Sci. Rep. 11 (1) (2021) 8745, https://doi.org/10.1038/s41598-021-88058-1.

[29] S. Chen, R. Zhao, Z. Xing, T. Shang, X. Yang, X. Zhu, X. Zhang, Strontium combined with bioceramics for osteoporotic bone repair: oral intake or as a dopant? Appl. Mater. Today 22 (2021), 100927 https://doi.org/10.1016/j.apmt.2020.100927.

[30] Z. Cai, J. Zhang, H. Li, Selenium, aging and aging-related diseases, Aging Clin. Exp. Res. 31 (8) (2019) 1035–1047, https://doi.org/10.1007/s40520-018-1086-7.

[31] Y. Wang, J. Wang, H. Hao, M. Cai, S. Wang, J. Ma, Y. Li, C. Mao, S. Zhang, In vitro and in vivo mechanism of bone tumor inhibition by selenium-doped bone mineral nanoparticles, ACS Nano 10 (11) (2016) 9927–9937, https://doi.org/10.1021/acsnano.6b03835.

[32] X. Li, Y. Wang, Y. Chen, P. Zhou, K. Wei, H. Wang, J. Wang, H. Fang, S. Zhang, Hierarchically constructed selenium-doped bone-mimetic nanoparticles promote ROS-mediated autophagy and apoptosis for bone tumor inhibition, Biomaterials 257 (2020), 120253, https://doi.org/10.1016/j.biomaterials.2020.120253.

[33] S. Muthusamy, B. Mahendiran, S. Sampath, S.N. Jaisankar, S. K. Anandasadagopan, G.S. Krishnakumar, Hydroxyapatite nanophases augmented with selenium and manganese ions for bone regeneration: physiochemical, microstructural and biological characterization, Mater. Sci. Eng., C 126 (2021), 112149, https://doi.org/10.1016/j.msec.2021.112149.

[34] D. Xiao, Z. Tan, Y. Fu, K. Duan, X. Zheng, X. Lu, J. Weng, Hydrothermal synthesis of hollow hydroxyapatite microspheres with nano-structured surface assisted by inositol hexakisphosphate, Ceram. Int. 40 (7) (2014) 10183–10188, https://doi.org/10.1016/j.ceramint.2014.02.057.

[35] J. Ortiz-Landeros, C. Gómez-Yáñez, R. López-Juárez, I. Dávalos-Velasco, H. Pfeiffer, Synthesis of advanced ceramics by hydrothermal crystallization and modified related methods, J. Adv. Ceram. 1 (3) (2012) 204–220, https://doi.org/10.1007/s40145-012-0022-0.

[36] S.P. Parthiban, I.Y. Kim, K. Kikuta, C. Ohtsuki, Effect of urea on formation of hydroxyapatite through double-step hydrothermal processing, Mater. Sci. Eng. C 31 (2011) 1383–1388, https://doi.org/10.1016/j.msec.2011.05.005.

[37] K. Hayashi, R. Kishida, A. Tsuchiya, K. Ishikawa, Honeycomb blocks composed of carbonate apatite, β-tricalcium phosphate, and hydroxyapatite for bone regeneration: effects of composition on biological responses, Materials, Today. Bio. 4 (2019), 100031. 10.1016/j.mtbio.2019.100031.

[38] H. Li, C. Zhang, Synthesis of Selenium Doped Hydroxyapatite via a Hydrothermal Procedure and the Experimental Study on Antitumor Effect, 2017. Chengdu.

[39] D.Q. Xiao, D.W. Wang, J.C. Ren, K. Duan, N. Yao, X. Lu, Xi T. Zheng, J. Weng, Synthesis and characterization of copper-substituted hydroxyapatite micrspheres, J. Inorg. Mater. 29 (7) (2014) 769–775, https://doi.org/10.3724/SP.J.1077.2014.13532.

[40] X. Zhou, C. Zhang, Hydrothermal Synthesis of Inorganic Ion Doped Hydroxyapatite Microspheres and Biological Properties Evaluation, 2015. Chengdu.

[41] L. He, J. Weng, Synthesis of Modified Hydroxyapatite via Incorporating Inorganic Trace Elements and the Related Biological Evaluation, 2019. Chengdu.

[42] L. He, H. Li, X. Chen, T. Xu, T. Sun, H. Huang, M. Lu, Y. Yin, J. Ge, J. Weng, N. Zhuo, K. Duan, Selenium-substituted hydroxyapatite particles with regulated microstructures for osteogenic differentiation and anti-tumor effects, Ceram. Int. 45 (11) (2019) 13787–13798, https://doi.org/10.1016/j.ceramint.2019.04.075.

[43] B. Priyadarshini, U. Vijayalakshmi, Development of cerium and silicon co-doped hydroxyapatite nanopowder and its in vitro biological studies for bone regeneration applications, Adv. Powder Technol. 29 (11) (2018) 2792–2803, https://doi.org/10.1016/j.apt.2018.07.028.

[44] D.K. Khajuria, V.B. Kumar, D. Gigi, A. Gedanken, D. Karasik, Accelerated bone regeneration by nitrogen-doped carbon dots functionalized with hydroxyapatite nanoparticles, ACS Appl. Mater. Interfaces 10 (23) (2018) 19373–19385, https://doi.org/10.1021/acsami.8b02792.

[45] H. Kim, S. Mondal, S. Bharathiraja, P. Manivasagan, M.S. Moorthy, J. Oh, Optimized Zn-doped hydroxyapatite/doxorubicin bioceramics system for efficient drug delivery and tissue engineering application, Ceram. Int. 44 (6) (2018) 6062–6071, https://doi.org/10.1016/j.ceramint.2017.12.235.

[46] A. Pal, P. Nasker, S. Paul, A. Choudhury, A. Sinha, M. Das, Strontium doped hydroxyapatite from Mercenaria clam shells: synthesis, mechanical and bioactivity study, J. Mech. Behav. Biomed. Mater. 90 (2019) 328–336, https://doi.org/10.1016/j.jmbbm.2018.10.027.

[47] Z. Geng, L. Ji, Z. Li, J. Wang, H. He, Z. Cui, X. Yang, C. Liu, Nano-needle strontium-substituted apatite coating enhances osteoporotic osseointegration through promoting osteogenesis and inhibiting osteoclastogenesis, Bioact. Mater. 6 (40) (2021) 905–915, https://doi.org/10.1016/j.bioactmat.2020.09.024.

[48] B. Liu, X. Shi, G. Xiao, Y. Lu, In-situ preparation of scholzite conversion coatings on titanium and Ti-6Al-4V for biomedical applications, Colloids, Surfnet Bull. 153 (2017) 291–299, https://doi.org/10.1016/j.colsurfb.2017.03.007.

[49] A. Szczes, L. Holysz, E. Chibowski, Synthesis of hydroxyapatite for biomedical applications, Adv. Colloid Interface Sci. 249 (2017) 321–330, https://doi.org/10.1016/j.cis.2017.04.007.

[50] W. Zhang, Z. Li, Q. Huang, L. Xu, J. Li, Y. Jin, G. Wang, X. Liu, X. Jiang, Effects of a hybrid micro/nanorod topography-modified titanium implant on adhesion and osteogenic differentiation in rat bone marrow mesenchymal stem cells, Int. J. Nanomed. 8 (2013) 257–265, https://doi.org/10.2147/ijn.s39357.

[51] M. Nouri-Felekori, M. Khakbiz, N. Nezafati, Synthesis and characterization of Mg, Zn and Sr-incorporated hydroxyapatite whiskers by hydrothermal method, Mater. Lett. 243 (2019) 120–124. 10.1016/j.matlet.2019.01.147.

[52] D. Fan, S. Wei, M. Ma, Z. Chen, B. Li, H. Xie, High-pressure elastic behavior of Ca4La6(SiO4)6(OH)2 a synthetic rare-earth silicate apatite: a powder X-ray diffraction study up to 9.33 GPa, Phys. Chem. Miner. 41 (2) (2013) 85–90, https://doi.org/10.1007/s00269-013-0626-0.

[53] G. Karunakaran, G.S. Kumar, E.-B. Cho, Y. Sunwoo, E. Kolesnikov, D. Kuznetsov, Microwave-assisted hydrothermal synthesis of mesoporous carbonated hydroxyapatite with tunable nanoscale characteristics for biomedical applications, Ceram. Int. 45 (1) (2019) 970–977, https://doi.org/10.1016/j.ceramint.2018.09.273.

[54] Ma Xiaomin, Peng Wanjia, Su Wen, Yi Zeng, G. C, X. Chen, Y. Chen, B. Guo, X. D. Li, Delicate assembly of ultrathin hydroxyapatite nanobelts with nanoneedles directed by dissolved cellulose, Inorg. Chem. 57 (8) (2018) 4516–4523, https://doi.org/10.1021/acs.inorgchem.8b00275.

[55] J. Guo, X. Liao, M.-H. Lee, G. Hyett, C.-C. Huang, D.W. Hewak, S. Mailis, W. Zhou, Z. Jiang, Experimental and DFT insights of the Zn-doping effects on the visible-light photocatalytic water splitting and dye decomposition over Zn-doped BiOBr photocatalysts, Appl. Catal., B 243 (2019) 502–512, https://doi.org/10.1016/j.apcatb.2018.09.089.

[56] X. Hao, J. Zhou, Z. Cui, Y. Wang, Y. Wang, Z. Zou, Zn-vacancy mediated electron-hole separation in ZnS/g-C3N4 heterojunction for efficient visible-light photocatalytic hydrogen production, Appl. Catal., B 229 (2018) 41–51, https://doi.org/10.1016/j.apcatb.2018.02.006.

[57] W.H. Lee, C.Y. Loo, R. Rohanizadeh, A review of chemical surface modification of bioceramics: effects on protein adsorption and cellular response, Colloids Surf. B Biointerfaces 122 (2014) 823–834, https://doi.org/10.1016/j.colsurfb.2014.07.029.

[58] C. Qi, Y.J. Zhu, B.Q. Lu, X.Y. Zhao, J. Zhao, F. Chen, J. Wu, Hydroxyapatite hierarchically nanostructured porous hollow microspheres: rapid, sustainable microwave-hydrothermal synthesis by using creatine phosphate as an organic phosphorus source and application in drug delivery and protein, Adsorption 19 (17) (2013) 5332–5341, https://doi.org/10.1002/chem.201203886.

[59] I. Ullah, M.A. Siddiqui, S.K. Kolawole, H. Liu, J. Zhang, L. Ren, K. Yang, Synthesis, characterization and in vitro evaluation of zinc and strontium binary doped hydroxyapatite for biomedical application, Ceram. Int. 46 (10) (2020) 14448–14459, https://doi.org/10.1016/j.ceramint.2020.02.242.

[60] W. Wang, K.W.K. Yeung, Bone grafts and biomaterials substitutes for bone defect repair: a review, Bioact. Mater. 2 (4) (2017) 224–247, https://doi.org/10.1016/j.bioactmat.2017.05.007.

[61] T. Chantapakul, R. Lv, W. Wang, W. Chummalee, T. Ding, D. Liu, Manothermosonication: inactivation of Escherichia coli and Staphylococcus aureus, J. Food Eng. 246 (2019) 16–24, https://doi.org/10.1016/j.jfoodeng.2018.10.009.

[62] M. Maqbool, Q. Nawaz, M. Atiq Ur Rehman, M. Cresswell, P. Jackson, K. Hurle, R. Detsch, W.H. Goldmann, A.T. Shah, A.R. Boccaccini, Synthesis, characterization, antibacterial properties, and in vitro studies of selenium and strontium Co-substituted hydroxyapatite, Int. J. Mol. Sci. 22 (8) (2021), https://doi.org/10.3390/ijms22084246.

[63] Q. Wang, P. Tang, X. Ge, P. Li, C. Lv, M. Wang, K. Wang, L. Fang, X. Lu, Experimental and simulation studies of strontium/zinc-codoped hydroxyapatite porous scaffolds with excellent osteoinductivity and antibacterial activity, Appl. Surf. Sci. 462 (2018) 118–126, https://doi.org/10.1016/j.apsusc.2018.08.068.

[64] A.S. Prasad, Genetic, N. A. o. Major, T. Minerals, Discovery of zinc for human health and biomarkers of zinc deficiency, in: Molecular, Genetic, and Nutritional Aspects of Major and Trace Minerals, 2017, pp. 241–260, https://doi.org/10.1016/B978-0-12-802168-2.00020-8. Detroit.

[65] G. Yao, J. Lei, W. Zhang, C. Yu, Z. Sun, S. Zheng, S. Komarneni, Antimicrobial activity of X zeolite exchanged with $Cu^{(2+)}$ and $Zn^{(2+)}$ on Escherichia coli and Staphylococcus aureus, Environ. Sci. Pollut. Res. Int. 26 (3) (2019) 2782–2793, https://doi.org/10.1007/s11356-018-3750-z.

[66] M.B. Dolic, V.N. Rajakovic-Ognjanovic, S.B. Strbac, S.I. Dimitrijevic, M.N. Mitric, A.E. Onjia, L.V. Rajakovic, Natural sorbents modified by divalent $Cu^{(2+)}$- and $Zn^{(2+)}$- ions and their corresponding antimicrobial activity, Nat. Biotechnol. 39 (Pt A) (2017) 150–159, https://doi.org/10.1016/j.nbt.2017.03.001.

[67] H. Yang, X. Qu, W. Lin, C. Wang, D. Zhu, K. Dai, Y. Zheng, In vitro and in vivo studies on zinc-hydroxyapatite composites as novel biodegradable metal matrix composite for orthopedic applications, Acta Biomater. 71 (2018) 200–214, https://doi.org/10.1016/j.actbio.2018.03.007.

[68] J. Jiang, G. Han, X. Zheng, G. Chen, P. Zhu, Surface characterization and biocompatibility of selenium-doped hydroxyapatite coating on titanium alloy, Int. J. Appl. Ceram. Technol. 13 (6) (2016) 1059–1068, https://doi.org/10.1016/j.surfcoat.2019.07.067.

[69] L. Wei, H. Yang, J. Hong, Z. He, C. Deng, Synthesis and structure properties of Se and Sr co-doped hydroxyapatite and their biocompatibility, J. Mater. Sci. 54 (3) (2018) 2514–2525, https://doi.org/10.1007/s10853-018-2951-7.

[70] V. Gandina, P. Khalkarb, J. Braudea, A.P. Fernandes, Organic selenium compounds as potential chemotherapeutic agents for improved cancer treatment, Free Radical Biol. Med. 127 (2018) 80–97, https://doi.org/10.1016/j.freeradbiomed.2018.05.001.

[71] S. Khan, M.W. Ullah, R. Siddique, Y. Liu, I. Ullah, M. Xue, G. Yang, H. Hou, Catechins-modified selenium-doped hydroxyapatite nanomaterials for improved osteosarcoma therapy through generation of reactive oxygen species, Front. Oncol. 9 (2019) 499, https://doi.org/10.3389/fonc.2019.00499.

[72] X. Ding, X. Li, C. Li, M. Qi, Z. Zhang, X. Sun, L. Wang, Y. Zhou, Chitosan/dextran hydrogel constructs containing strontium-doped hydroxyapatite with enhanced osteogenic potential in rat cranium, ACS Biomater. Sci. Eng. 5 (9) (2019) 4574–4586, https://doi.org/10.1021/acsbiomaterials.9b00584.

[73] L. Stipniece, S. Wilson, J.M. Curran, R. Chen, K. Salma-Ancane, P.K. Sharma, B. J. Meenan, A.R. Boyd, Strontium substituted hydroxyapatite promotes direct primary human osteoblast maturation, Ceram. Int. 47 (3) (2021) 3368–3379, https://doi.org/10.1016/j.ceramint.2020.09.182.

[74] E. Mavropoulos, M. Hausen, A.M. Costa, G. Alves, A. Mello, C.A. Ospina, M. Mir, J.M. Granjeiro, A.M. Rossi, The impact of the RGD peptide on osteoblast adhesion and spreading on zinc-substituted hydroxyapatite surface, J. Mater. Sci. Mater. Med. 24 (5) (2013) 1271–1283, https://doi.org/10.1007/s10856-013-4851-3.

[75] S. Zakhireh, K. Adibkia, Y. Beygi-Khosrowshahi, M. Barzegar-Jalali, Osteogenesis promotion of selenium-doped hydroxyapatite for application as bone scaffold, Biol. Trace Elem. Res. 199 (5) (2021) 1802–1811, https://doi.org/10.1007/s12011-020-02309-2.

[76] Y. Li, W. Wang, J. Han, Z. Li, Q. Wang, X. Lin, K. Ge, G. Zhou, Synthesis of silver- and strontium-substituted hydroxyapatite with combined osteogenic and antibacterial activities, Biol. Trace Elem. Res. 200 (2) (2021) 931–942, https://doi.org/10.1007/s12011-021-02697-z.

[77] K. Xiong, J. Zhang, Y. Zhu, L. Chen, J. Ye, Zinc doping induced differences in the surface composition, surface morphology and osteogenesis performance of the calcium phosphate cement hydration products, Mater. Sci. Eng., C 105 (2019), 110065, https://doi.org/10.1016/j.msec.2019.110065.

[78] Y. Li, H. Hao, Z. Zhong, M. Li, J. Li, Y. Du, S. Zhang, Assembly mechanism of highly crystalline selenium-doped hydroxyapatite nanorods via particle attachment and their effect on the fate of stem cells, ACS Biomater. Sci. Eng. 5 (12) (2019) 6703–6714, https://doi.org/10.1021/acsbiomaterials.9b01029.

[79] D. Liu, W. Nie, D. Li, W. Wang, L. Zheng, J. Zhang, J. Zhang, C. Peng, X. Mo, C. He, 3D printed PCL/SrHA scaffold for enhanced bone regeneration, Chem. Eng. J. 362 (2019) 269–279, https://doi.org/10.1016/j.cej.2019.01.015.

[80] H. Maleki-Ghaleh, M. Siadati, Y. Beygi-Khosrowshahi, K. Adibkia, Effect of zinc-doped hydroxyapatite/graphene nanocomposite on the physicochemical properties and osteogenesis differentiation of 3D-printed polycaprolactone scaffolds for bone tissue engineering, Chem. Eng. J. 426 (2021), 131321, https://doi.org/10.1016/j.cej.2021.131321.

[81] H. Cheng, R. Chabok, X. Guan, A. Chawla, Y. Li, A. Khademhosseini, H.L. Jang, Synergistic interplay between the two major bone minerals, hydroxyapatite and whitlockite nanoparticles, for osteogenic differentiation of mesenchymal stem cells, Acta Biomater. 69 (2018) 342–351, https://doi.org/10.1016/j.actbio.2018.01.016.

[82] G.X. Ni, K.Y. Chiu, W.W. Lu, Y. Wang, Y.G. Zhang, L.B. Hao, Z.Y. Li, W.M. Lam, S. B. Lu, K.D.K. Luk, Strontium-containing hydroxyapatite bioactive bone cement in revision hip arthroplasty, Biomaterials 27 (24) (2006) 4348–4355, https://doi.org/10.1016/j.biomaterials.2006.03.048.

[83] Y. Zhu, K. Zhang, R. Zhao, X. Ye, X. Chen, Z. Xiao, X. Yang, X. Zhu, K. Zhang, Y. Fan, X. Zhang, Bone regeneration with micro/nano hybrid-structured biphasic calcium phosphate bioceramics at segmental bone defect and the induced immunoregulation of MSCs, Biomaterials 147 (2017) 133–144, https://doi.org/10.1016/j.biomaterials.2017.09.018.

[84] M. Zhang, Z. Gong, J. Zhang, H. Cheng, J. Chen, Y. Zeng, Z. Zhu, Y. Wan, Engineered zinc titanate coatings on the titanium surface with enhanced antitumor properties and biocompatibility, ACS Biomater. Sci. Eng. 5 (11) (2019) 5935–5946, https://doi.org/10.1021/acsbiomaterials.9b00841.

[85] M.E. Karim, J. Shetty, R.A. Islam, A. Kaiser, E.H. Chowdhury, Strontium sulfite: a new pH-responsive inorganic nanocarrier to deliver therapeutic siRNAs to cancer cells, Pharmaceutics 11 (2) (2019) 89, https://doi.org/10.3390/pharmaceutics11020089.

[86] H. Yan, H. Chang, Antioxidant and antitumor activities of selenium- and zinc-enriched oyster mushroom in mice, Biol. Trace Elem. Res. 150 (1–3) (2012) 236–241, https://doi.org/10.1007/s12011-012-9454-1.

[87] N. Gómez-Cerezo, L. Casarrubios, M. Saiz-Pardo, L. Ortega, Mesoporous bioactive glass/ε-polycaprolactone scaffolds promote bone regeneration in osteoporotic sheep, Acta Biomater. 90 (2019) 393–402, https://doi.org/10.1016/j.actbio.2019.04.019.

[88] K. Gómez-Lizárraga, C. Flores-Morales, M. Prado-Audelo, M. Álvarez-Pérez, M. Piña-Barba, C. Escobedo, Polycaprolactone- and polycaprolactone/ceramic-based 3D-bioplotted porous scaffolds for bone regeneration: a comparative study, Mater. Sci. Eng. C 79 (2017) 326–335, https://doi.org/10.1016/j.msec.2017.05.003.

[89] E. Backes, C. Beatrice, K. Shimomura, L. Pessan, Development of poly(Ɛ-polycaprolactone)/hydroxyapatite composites for bone tissue regeneration, J. Mater. Res. 36 (2021) 3050–3062, https://doi.org/10.1557/s43578-021-00316-0.

[90] V. Karageorgiou, D. Kaplan, Porosity of 3D biomaterial scaffolds and osteogenesis, Biomaterials 26 (27) (2005) 5474–5491, https://doi.org/10.1016/j.biomaterials.2005.02.002.
[91] Y. Hou, L. Yu, W. Xie, L.C. Camacho, M. Zhang, Z. Chu, Q. Wei, R. Haag, Surface roughness and substrate stiffness synergize to drive cellular mechanoresponse, Nano Lett. 20 (1) (2020) 748–757, https://doi.org/10.1021/acs.nanolett.9b04761.
[92] Z. Ebrahimi, S. Irani, A. Ardeshirylajimi, E. Seyedjafari, Enhanced osteogenic differentiation of stem cells by 3D printed PCL scaffolds coated with collagen and hydroxyapatite, Sci. Rep. 12 (2022), 12359, https://doi.org/10.1038/s41598-022-15602-y.
[93] N. Pattanashetti, T. Viana, G. Mitchell, M. Kariduraganavar, Development of novel 3D scaffolds using BioExtruder by varying the content of hydroxyapatite and silica in PCL matrix for bone tissue engineering, J. Polym. Res. 27 (2020) 87, https://doi.org/10.1007/s10965-020-02053-0.
[94] C. Zhao, X. Xu, Y. Lu, S. Wu, Z. Xu, T. Huang, J. Lin, Doping lithium element to enhance compressive strength of beta-TCP scaffolds manufactured by 3D printing for bone tissue engineering, J. Alloys Compd. 814 (2020), 152327, https://doi.org/10.1007/s10965-020-02053-0.
[95] K. Hiraoka, S. Komiya, T. Hamada, A. Inoue, Osteosarcoma cell apoptosis induced by selenium, J. Orthop. Res. 19 (2001) 809–814, https://doi.org/10.1016/s0736-0266(00)00079-6.
[96] H. Zhao, C. Wu, D. Gao, S. Chen, Y. Zhu, J. Sun, H. Luo, K. Yu, H. Fan, X. Zhang, Antitumor effect by hydroxyapatite nanospheres: activation of mitochondria-dependent apoptosis and negative regulation of phosphatidylinositol-3-kinase/protein kinase B pathway, ACS Nano 12 (8) (2018) 7838–7854, https://doi.org/10.1021/acsnano.8b01996.
[97] K. Gao, Y. Zhang, J. Niu, Z. Nie, Q. Liu, C. Lv, Zinc promotes cell apoptosis via activating the Wnt-3a/β-catenin signaling pathway in osteosarcoma, J. Orthop. Surg. Res. 199 (2019) 3222–3231, https://doi.org/10.1186/s13018-020-01585-x.
[98] V. Uskokovi, M. Iyer, V. Wu, One ion to rule them all: the combined antibacterial, osteoinductive and anticancer properties of selenite-incorporated hydroxyapatite, J. Mater. Chem. B 5 (7) (2017) 1430–1445, https://doi.org/10.1039/c6tb03387c.
[99] J. Wang, Q. Li, A. Bao, X. Liu, J. Zeng, X. Yang, J. Yao, J. Zhang, Z. Lei, Synthesis of selenium-containing Artemisia sphaerocephala polysaccharides: solution conformation and anti-tumor activities *in vitro*, Carbohydr. Polym. 152 (2016) 70–78, https://doi.org/10.1016/j.carbpol.2016.06.090.
[100] Y. Li, H. Hao, Z. Zhong, M. Li, S. Zhang, Assembly mechanism of high-crystallized selenium-doped hydroxyapatite nanorods via particle attachment and their effect on stem cells fate, ACS Biomater. Sci. Eng. 5 (12) (2019) 6703–6714, https://doi.org/10.1021/acsbiomaterials.9b01029.
[101] C. Vaquette, N. Bock, P. Tran, Layered antimicrobial selenium nanoparticle–calcium phosphate coating on 3D printed scaffolds enhanced bone formation in critical size defects, ACS Appl. Mater. Interfaces 12 (50) (2020) 55638–55648, https://doi.org/10.1021/acsami.0c17017.
[102] A. Hosseinzadeh, S. Hosseini-Asl, M. Mohammadzadeh-Vardin, M. Sagha, The telomerase activity of selenium-induced human umbilical cord mesenchymal stem cells is associated with different levels of c-myc and p53 expression, DNA Cell Biol. 36 (1) (2017) 34, https://doi.org/10.1089/dna.2016.3411.
[103] M. Zimmerman, C. Bayse, R. Ramoutar, J. Brumaghim, Sulfur and selenium antioxidants: challenging radical scavenging mechanisms and developing structure-activity relationships based on metal binding, J. Inorg. Biochem. 145 (2015) 30–40, https://doi.org/10.1016/j.jinorgbio.2014.12.020.
[104] P. Habibovic, J. Barralet, Bioinorganics and biomaterials: bone repair, Acta Biomater. 7 (8) (2011) 3013–3026, https://doi.org/10.1016/j.actbio.2011.03.027.
[105] L. Zhao, H. Wang, K. Huo, X. Zhang, Z. Wu, P. Chu, The osteogenic activity of strontium loaded titania nanotube arrays on titanium substrates, Biomaterials 34 (1) (2013) 19–29, https://doi.org/10.1016/j.biomaterials.2012.09.041.
[106] C. Chasapis, A. Loutsidou, C. Spiliopoulou, M. Stefanidou, Zinc in human health: an update, Arch. Toxicol. 86 (1998) 521–534, https://doi.org/10.1007/s00204-011-0775-1.
[107] M. Yamaguchi, M. Weitzmann, Zinc stimulates osteoblastogenesis and suppresses osteoclastogenesis by antagonizing NF-κB activation, Mol. Cell. Biochem. 355 (2011) 179–186, https://doi.org/10.1007/s11010-011-0852-z.